

Fifth order multi-moment WENO schemes for hyperbolic conservation laws

Chieh-Sen Huang · Feng Xiao · Todd Arbogast

Received: May 2014 / Accepted: not yet

Abstract A general approach is given to extend WENO reconstructions to a class of numerical schemes that use different types of moments (i.e., multi-moments) simultaneously as the computational variables, such as point values and grid cell averages. The key is to re-map the multi-moment values to single moment values (e.g., cell average or point values), which can then be used to invoke known, standard reconstruction coefficients and smoothness indicators for single moment WENO reconstructions. The WENO reconstructions in turn provide the numerical approximations for the flux functions and other required quantities. One major advantage of using multi-moments for WENO reconstructions is its compactness. We present two new multi-moment WENO (MM-WENO) schemes of fifth order that use reconstructions supported over only three grid cells, as opposed to the usual five. This is similar to the Hermite WENO schemes of Qiu and Shu [J. Comput. Phys. 193 (2003)], which can also be derived using our general approach. Numerical tests demonstrate that the new schemes achieve their designed fifth order accuracy and eliminate spurious oscillations effectively. The numerical solutions to all benchmark tests are of good quality and comparable to the classic, single moment WENO scheme of the same order of accuracy. The basic idea presented in this paper is universal, which makes the WENO reconstruction an easy-to-follow method for developing a wide variety of additional multi-moment numerical schemes.

Authors supported in part for the first under Taiwan National Science Council grant NSC 99-2115-M-110-006-MY3; the second by JSPS KAKENHI (24560187); and the third as part of the Center for Frontiers of Subsurface Energy Security, an Energy Frontier Research Center funded by the U.S. Department of Energy under Award Number DE-SC0001114, and by the U.S. National Science Foundation grant DMS-0835745.

Chieh-Sen Huang

Department of Applied Mathematics and National Center for Theoretical Sciences, National Sun Yat-sen University, Kaohsiung 804, Taiwan, R.O.C.
E-mail: huangcs@math.nsysu.edu.tw

Feng Xiao

Tokyo Institute of Technology, 4259 Nagatsuta, Midori-ku, Yokohama, 226-8502, Japan
E-mail: xiao@es.titech.ac.jp

Todd Arbogast

University of Texas at Austin, Institute for Computational Engineering and Sciences, 201 EAST 24th St., Stop C0200, Austin, Texas 78712-1229 USA
E-mail: arbogast@ices.utexas.edu

Keywords WENO reconstruction · multi-moment · MM-WENO scheme · hyperbolic conservation law · finite volume · finite difference · Hamilton-Jacobi equation · Euler equations

Mathematics Subject Classification (2000) 65M06 · 65M08 · 76M12 · 76M20

1 Introduction

The weighted essentially nonoscillatory (WENO) [14, 13, 16, 9] method is one of the more popular numerical methods for convection dominated problems, such as the hyperbolic conservation law

$$\frac{\partial u}{\partial t} + \frac{\partial f(u)}{\partial x} = 0, \quad x \in \mathbb{R}, t > 0, \quad (1)$$

for the solution u with the given flux function $f(u; x, t)$, when the solution has spatial discontinuities but is otherwise smooth. A WENO scheme can achieve high order formal accuracy for the smooth part of the solution while effectively suppressing spurious oscillations that are always generated around discontinuities when using more than linear degree polynomial reconstruction. Moreover, WENO schemes are *almost* optimized in the sense that there are no parameters that need to be adjusted. WENO schemes can be derived in terms of approximations of either point values of the solution (i.e., finite differences) [16] or volume-integrated cell averages of the solution (i.e., finite volumes) [16].

A class of numerical schemes, the multi-moment finite volume methods (MMFVM) [22, 18–20, 10, 3, 11, 1], have recently been devised to solve general hyperbolic conservation laws. The underlying idea traces back to the constrained interpolation profile (CIP) method [26]. In a multi-moment scheme, one makes use of various kinds of discrete quantities approximating the solution, such as pointwise values (PV), pointwise derivative values (PDV), and volume-integrated average values (AV), which are termed “moments” in our context. These are updated simultaneously at every time step. By using multiple locally defined moments, high-order schemes can be constructed over a relatively compact stencil. The temporal evolution equations used to update different moments can take different forms, but each must be consistent with the original conservation law. By properly choosing the moments, one can construct high order numerical schemes with desired properties in an intuitive and physics-compatible way. As an example, one might use the AV moment to introduce a finite volume formulation, thus realizing numerical conservation, and supplement this with the PV moment to incorporate a (semi) Lagrangian mapping along characteristic trajectories to achieve a larger stable CFL number and reduce numerical dispersion. As shown in previous works, the multi-moment method provides flexible, efficient and accurate numerical formulations to computational fluid dynamics and other applications.

The Hermite WENO scheme of Qiu and Shu [15] was devised to make use of approximations to both point values and first-order derivatives of the solution, resulting in a WENO scheme that has a more compact grid stencil than a straightforward finite difference or volume scheme. It can be viewed as a type of multi-moment scheme, but within a WENO framework. In this direction, we propose in this paper a general framework for combining multi-moment and WENO ideas, resulting in multi-moment WENO (MM-WENO) schemes.

In past work involving the MMFVM, limiting projections to suppress numerical oscillations have been devised by using rational functions [23, 24], slope limiters [18, 19, 1] and total variation bounded (TVB) limiters [10, 11]. In this paper, we will suppress numerical

oscillations in multi-moment methods by using WENO reconstructions. In general, formulas for WENO reconstructions, linear weights, and smoothness indicators must be devised for each set of multi-moments. We avoid this technical complexity by re-mapping multi-moment values to cell integrated average values (AV) or point values (PV). We do this by relating multi-moment basis functions to single moment basis functions in terms of either AV or PV, and thereby convert information to the single moment framework. Since the classic finite volume (AV) or finite difference (PV) WENO scheme is known, we can make use of the classic WENO formulas to define the reconstruction polynomials and smoothness indicators. The latter, in particular, greatly simplifies the derivation of the MM-WENO scheme.

We present two new multi-moment WENO schemes for our problem (1) that are of formal fifth order accuracy and that we believe are useful in practical computations. These combine AV and PV multi-moments to achieve conservative finite volume schemes for the AV moments and use only stencils supported on a set of three grid elements, which is more compact than standard fifth order WENO schemes, which use five. The evolution of point values is based either on a Hamilton-Jacobi formulation of the equation [12] or on a more traditional finite difference form [16], which results in two schemes, the MM-WENO-HJ scheme and the MM-WENO-FD scheme, respectively.

We demonstrate that the basic idea of introducing WENO reconstructions into a multi-moment scheme is universal as long as a proper re-mapping formulation is determined. We also show that the Hermite WENO [15] can be interpreted within this framework, where we start with the moments AV and volume-integrated averages of the derivative value (ADV).

The rest of paper is organized as follows. The re-mapping procedures that relate multi-moment values to single moment values is described in a general way in Section 2. The re-mapping formulation amounts to a change of basis, and it allow us to re-use single moment WENO reconstructions in a straightforward way. The two new MM-WENO schemes are given in Section 3. In Section 4, the specific WENO reconstructions needed by our two MM-WENO schemes are given in detail. The re-mapping, change of basis matrices are given, as well as the coefficients of the stencil polynomials, the smoothness indicators, and the linear weights needed in the WENO reconstruction. We relate the ideas to the Hermite-WENO scheme in Section 5, where we give the change of basis matrices needed for mapping AV and ADV moments to single moments AV or PV. Section 6 gives numerical results of some benchmark tests to verify the convergence rate and the oscillation suppression properties of the proposed schemes. We show that the new schemes achieve their designed fifth order accuracy and eliminate spurious oscillations effectively. The numerical solutions are all of good quality and comparable to the classic, single moment WENO scheme of the same order of accuracy. An extension to the Euler equations of gas dynamics is presented in Section 7 with numerical examples. We end this paper with a summary and conclusions in the last section.

2 Abstract framework for multi-moment WENO reconstruction

Let us fix the notation for the computational grid. Various boundary conditions and nonuniform grids could be handled by our techniques, provided that they can be handled by the associated single moment WENO reconstructions, and they would be handled in the same way. However, for simplicity of exposition of the ideas, we assume periodic boundary conditions and choose a uniform spatial grid. So fix the spacing $\Delta x > 0$ and set the grid points as $x_{i-1/2} := (i - 1/2)\Delta x$ and the central points to be $x_i := i\Delta x$. The i th grid element is then

$E_i := [(i - 1/2)\Delta x, (i + 1/2)\Delta x] = [x_{i-1/2}, x_{i+1/2}]$, and its center is x_i . For non-integral k , $x_k := k\Delta x$ as well.

2.1 General WENO reconstruction from multi-moments

In order to describe general multi-moment WENO reconstructions, we define a *moment* of a smooth function u defined on \mathbb{R} to be the value of a linear functional \mathcal{L} applied to u . We tacitly assume that our moments are locally defined in the sense that \mathcal{L} is supported on a single element E_i (i.e., $\mathcal{L}(u) = \mathcal{L}(u|_{E_i})$). For example, $u(x)$ may be approximated on E_i by its element averages (AV moments)

$$\bar{u}_i \approx \frac{1}{\Delta x} \int_{x_{i-1/2}}^{x_{i+1/2}} u(x) dx, \quad (2)$$

or by its grid point values at either endpoint (PV moments), such as

$$u_{i+1/2} \approx u(x_{i+1/2}). \quad (3)$$

The function derivative $u'(x)$ may be approximated on E_i by its element averages (average derivative values or ADV moments)

$$(\bar{u}_x)_i \approx \frac{1}{\Delta x} \int_{x_{i-1/2}}^{x_{i+1/2}} u'(x) dx = \frac{u(x_{i+1/2}) - u(x_{i-1/2})}{\Delta x}, \quad (4)$$

or by its grid point derivative values (PDV moments)

$$u_{x,i+1/2} \approx u'(x_{i+1/2}). \quad (5)$$

In general, now, suppose that we have a set of M linearly independent linear functionals $\{\mathcal{L}_1, \mathcal{L}_2, \dots, \mathcal{L}_M\}$, ordered so the supports move from left to right. The corresponding multi-moment values are $\mathcal{M} := \{m_1, m_2, \dots, m_M\}$, where $m_i \approx \mathcal{L}_i(u)$ is a numerical approximation to the true moment. We divide these moments into overlapping subsets or stencils of equal size s . There will be $N = M - s + 1$ such stencils, which we denote by

$$\mathcal{M}_j := \{m_j, m_{j+1}, \dots, m_{j+s-1}\}, \quad j = 1, 2, \dots, N. \quad (6)$$

The WENO reconstruction will target high-order approximation of a fixed given linear functional $\mathcal{L}(u)$, which may be any of the types of moments above or possibly the value of u at a point other than a grid point. WENO reconstruction has essentially three steps.

In the first step, we need to reconstruct the N polynomials of degree $s - 1$ that match the moments over the stencil. That is, we need each stencil polynomial $q_j \in \mathbb{P}^{s-1}$ such that

$$\mathcal{L}_i(q_j) = m_i, \quad i = j, j + 1, \dots, j + s - 1, \quad j = 1, 2, \dots, N. \quad (7)$$

The linear independence of the multi-moments means that these polynomials are defined uniquely. As part of the first step and to complete the next step, we also need the polynomial of degree $M - 1$ that matches all the moments. This is $q \in \mathbb{P}^{M-1}$ such that

$$\mathcal{L}_i(q) = m_i, \quad i = 1, 2, \dots, M. \quad (8)$$

Again, the linear independence of the multi-moments means that q is defined uniquely.

The second step is to determine the linear weights needed for high-order reconstruction. Each q_i is accurate to $\mathcal{O}(\Delta x^s)$ but q is $\mathcal{O}(\Delta x^M)$. We need to find the linear weights γ_j so that

$$\mathcal{L}(q) = \sum_{j=1}^N \gamma_j \mathcal{L}(q_j) \quad (9)$$

for any possible instance of the moments \mathcal{M} . This is an overdetermined system, and so linear weights do not exist for every choice of target functional \mathcal{L} . If the linear weights do not exist, we cannot continue in the standard WENO framework (but see [8, 7] for a re-averaging technique to circumvent this problem). If they do exist, and assuming that \mathcal{L} is bounded in the appropriate norm, the value $\mathcal{L}(q)$ can be computed as $\sum_{j=1}^N \gamma_j \mathcal{L}(q_j)$ with accuracy $\mathcal{O}(\Delta x^M)$.

The third and final step is to compute the nonlinear weights as a modification of the linear weights. The purpose is to weight away from stencils that cross discontinuities in the solution. To this end, we define the standard indicator of smoothness over the element E_i (where \mathcal{L} is supported) as $IS_j^i(\Delta x)$, where

$$IS_j^i(h) := \sum_{\ell=1}^2 \int_{x_i-h/2}^{x_i+h/2} h^{2\ell-1} \left[\frac{\partial^\ell q_j(x)}{\partial x^\ell} \right]^2 dx, \quad j = 1, 2, \dots, N. \quad (10)$$

The nonlinear weights $\tilde{\gamma}_j^i$ are then

$$\tilde{\gamma}_j^i := \frac{\hat{\gamma}_j^i}{\sum_{k=1}^N \hat{\gamma}_k^i}, \quad \text{where} \quad \hat{\gamma}_k^i := \frac{\gamma_k}{(\varepsilon + IS_k^i)^2}, \quad j, k = 1, 2, \dots, N, \quad (11)$$

and $\varepsilon > 0$ is small, taken to be 10^{-6} in our numerical tests. Finally, the WENO reconstruction of $\mathcal{L}(u)$ is given as

$$\mathcal{L}(u) \approx \sum_{j=1}^N \tilde{\gamma}_j^i \mathcal{L}(q_j). \quad (12)$$

2.2 The re-mapping procedure

In general, step three is perhaps the most difficult to compute, because it involves an integral of a square of derivatives of the stencil polynomials. It has been computed for standard WENO schemes using single moments based on PVs or AVs [13, 16]. We describe a re-mapping technique that amounts to a change of basis to single moments and enables us to re-use this knowledge and thereby greatly simplify the computation of step three. Step one can be simplified as well. Unfortunately, the second step of finding the linear weights must be worked out for each choice of multi-moments.

We re-map each set of multi-moments $\mathcal{M}_j = \{m_j, m_{j+1}, \dots, m_{j+s-1}\}$ for the j th stencil to a set of standard PV or AV moments $\{v_j^j, v_{j+1}^j, \dots, v_{j+s-1}^j\}$, defined on either an extended or a refined grid so as to match the number of degrees of freedom s . We can do this by a change of basis. We construct two bases for \mathbb{P}^{s-1} , the multi-moment standard basis $\{\phi_1^j, \dots, \phi_s^j\}$ satisfying

$$\mathcal{L}_{j+k-1}(\phi_i^j) = \delta_{ik}, \quad i, k = 1, \dots, s, \quad j = 1, \dots, N, \quad (13)$$

and the single moment standard basis $\{\Phi_1^j, \dots, \Phi_s^j\}$ (e.g., this is the Lagrange basis for PV moments), which can be constructed directly or by invoking standard formula. The change of basis matrix $B^j = (b_{ik}^j)$ is then defined by expanding each ϕ_i^j in the standard basis, i.e.,

$$\phi_i^j(x) = \sum_{k=1}^s b_{ik}^j \Phi_k^j(x), \quad i = 1, \dots, s,$$

and the vector of multi-moments \mathbf{m}^j are re-mapped to the vector of standard moments \mathbf{v}^j as

$$\mathbf{v}^j = B^T \mathbf{m}^j. \quad (14)$$

We can compute the polynomial $q_j(x)$ in any of three ways:

$$q_j(x) = \sum_{i=1}^s v_{j+i-1}^j \Phi_i^j(x) = \sum_{i=1}^s (B^T \mathbf{m}^j)_i \Phi_i^j(x) = \sum_{i=1}^s m_{j+i-1}^j \phi_i^j(x). \quad (15)$$

There appears to be no advantage to any of the formulas for this purpose. However, the first formula, expansion in terms of the single moments, makes it easier to compute the smoothness indicator (10), since standard formula can be invoked for the single moments $\mathbf{v}^j = B^T \mathbf{m}^j$. We remark that the single moments are defined locally over the stencil and most likely do not form a global set of moments that can be used to describe q . This prevents us from using a standard formula for the linear weights (9).

3 Multi-moment WENO schemes for a scalar conservation law

As mentioned, different schemes can be constructed using the multi-moment concept. In this paper, we use the two moments AV and PV defined in (2) and (3), respectively, as the computational variables to be updated every time step. That is, we use moment unknowns consisting of a cell average \bar{u}_i over each grid element and a point value $u_{i+1/2}$ at each grid point. The solution procedure is described below, with the WENO reconstructions discussed abstractly in the previous section and to be elaborated on more concretely in the next section. The resulting scheme is referred to as the Multi-Moment WENO (MM-WENO) scheme.

Given $f(u; x, t)$, consider the initial value problem for a hyperbolic conservation law

$$\frac{\partial u}{\partial t} + \frac{\partial f(u)}{\partial x} = 0, \quad x \in \mathbb{R}, t > 0, \quad (16)$$

$$u(x, 0) = u_0(x), \quad x \in \mathbb{R}. \quad (17)$$

As a multi-moment scheme, we need evolution equations for both AVs and PVs, which can be written in the semidiscrete in space form

$$\frac{d\bar{u}_i}{dt} = -\frac{1}{\Delta x} (\hat{f}_{i+1/2} - \hat{f}_{i-1/2}), \quad (18)$$

$$\frac{du_{i+1/2}}{dt} = -\hat{f}_{x, i+1/2}, \quad (19)$$

where \hat{f} and \hat{f}_x are the numerical fluxes that need to be chosen. Note that the AVs are updated in a conservative fashion.

For the AV evolution equation (18), it is standard to define

$$\hat{f}_{i+1/2} = \mathcal{H}(u_{i+1/2}^-, u_{i+1/2}^+), \quad (20)$$

with $u_{i+1/2}^\pm$ obtained by left and right WENO reconstructions, which we will derive in detail later in Subsection 4.1 (see (43)). The function \mathcal{H} could be taken as any monotone flux. We use the Lax-Friedrichs flux in our numerical tests.

Within the PV evolution equation (19), we have two natural choices for the function \hat{f}_x , which lead to two different MM-WENO schemes.

3.1 The MM-WENO-HJ scheme

The first choice for PV evolution is to consider (16) as a Hamilton-Jacobi (HJ) equation

$$\frac{du}{dt} = -H(u, u_x) := -(f_x(u) + f_u(u)u_x). \quad (21)$$

Then we can apply the HJ-WENO scheme of Jiang and Peng [12]. The semidiscrete form of the HJ-WENO scheme is

$$\frac{du_{i+1/2}}{dt} = -\hat{H}(u, u_{x,i+1/2}^+, u_{x,i+1/2}^-), \quad (22)$$

so that $\hat{f}_{x,i+1/2} = \hat{H}(u, u_{x,i+1/2}^+, u_{x,i+1/2}^-)$ in (19). Here, \hat{H} must be a Lipschitz continuous monotone flux consistent with H , and $u_{x,i+1/2}^\pm$ are obtained by left and right WENO reconstructions.

We take \hat{H} to be the Lax-Friedrichs flux, which in this case is

$$\hat{H}(u, u_x^+, u_x^-) = H\left(u, \frac{u_x^+ + u_x^-}{2}\right) - \alpha \frac{u_x^+ - u_x^-}{2}, \quad (23)$$

where

$$\alpha = \max_u |f_u(u)|, \quad (24)$$

over the relevant range of u , since $\frac{\partial H}{\partial u_x} = f_u(u)$. We call the scheme MM-WENO-HJ since the PVs in (19) are evolved by the HJ-WENO scheme. The reconstruction of $u_{x,i+1/2}^+$ and $u_{x,i+1/2}^-$ is described below in Subsection 4.2 (see (55) and (56), respectively).

3.2 The MM-WENO-FD scheme

We also define a version called MM-WENO-FD in which PVs are evolved by the standard finite difference (FD) WENO scheme of Shu [16]. We define the Lax-Friedrichs splitting by setting

$$f^\pm(u) = \frac{1}{2}(f(u) \pm \alpha u), \quad (25)$$

where α is given in (24). The global flux splitting is then defined as

$$f(u) = f^+(u) + f^-(u). \quad (26)$$

We apply the WENO reconstruction procedures defined later in Subsection 4.3 for a sliding average function $h(x)$ of $f(x)$. We use (73) and (74) to obtain $h_{i+3/4}^-$ and $h_{i+3/4}^+$

respectively, as well as $h_{i+1/4}^+$ and $h_{i+1/4}^-$ as computed from these equations by symmetry, respectively. We define the numerical fluxes

$$\hat{f}_{i+3/4}^\pm := h_{i+3/4}^\mp, \quad \hat{f}_{i+3/4} := \hat{f}_{i+3/4}^+ + \hat{f}_{i+3/4}^- = h_{i+3/4}^- + h_{i+3/4}^+, \quad (27)$$

$$\hat{f}_{i+1/4}^\pm := h_{i+1/4}^\mp, \quad \hat{f}_{i+1/4} := \hat{f}_{i+1/4}^+ + \hat{f}_{i+1/4}^- = h_{i+1/4}^- + h_{i+1/4}^+. \quad (28)$$

The numerical flux needed in (19) is then

$$\hat{f}_{x,i+1/2} = \frac{2}{\Delta x} (\hat{f}_{i+3/4} - \hat{f}_{i+1/4}), \quad (29)$$

and the semidiscrete MM-WENO-FD scheme is completed.

The MM-WENO-FD scheme requires more computational steps than the MM-WENO-HJ scheme. Our MM-WENO-FD scheme requires WENO reconstructions at two points $x_{i+1/4}$ and $x_{i+3/4}$ for updating the PV at $x_{i+1/2}$, whereas, MM-WENO-HJ computes the fluxes only at $x_{i+1/2}$.

Remark. The computational costs of the MM-WENO schemes are of course higher than classic WENO schemes, as we need to update multi-moments. However, the extra moment information allows us to derive more flexible and accurate numerical formulations to computational fluid dynamics and other applications. In particular, our two new schemes achieve formal fifth order accuracy using a more compact stencil than classic single moment WENO schemes. By a more compact stencil, we mean that, although the stencil size is the same, the multi-moments are supported on a smaller region of the x -axis. The computational cost of MM-WENO-HJ is about the same as the Hermite WENO scheme.

3.3 Time integration

Finally, we discuss the time integration for a time step $\Delta t > 0$ from time t^n to t^{n+1} . We are now provided with the numerical fluxes on the right-hand sides of the semidiscrete AV and PV evolution equations (18) and (19). Therefore, both yield the following type of ordinary differential equation

$$\frac{dv}{dt} = L(v), \quad (30)$$

where v could be an AV or PV moment, and $L(v)$ is the right-hand side of either evolution equation. We use the third-order TVD Runge-Kutta scheme [13] for our numerical tests of the Euler equations, which is to compute the time integration as

$$\begin{cases} v^{(1)} = v^n + \Delta t L(v^n), \\ v^{(2)} = \frac{3}{4}v^n + \frac{1}{4}v^{(1)} + \frac{1}{4}\Delta t L(v^{(1)}), \\ v^{n+1} = \frac{1}{3}v^n + \frac{2}{3}v^{(2)} + \frac{2}{3}\Delta t L(v^{(2)}). \end{cases} \quad (31)$$

The non-TVD fourth-order Runge-Kutta scheme [13] is used for all other examples, which is to compute

$$\begin{cases} v^{(1)} = v^n + \frac{1}{2}\Delta t L(v^n), \\ v^{(2)} = v^n + \frac{1}{2}\Delta t L(v^{(1)}), \\ v^{(3)} = v^n + \Delta t L(v^{(2)}), \\ v^{n+1} = \frac{1}{3}(-v^n + v^{(1)} + 2v^{(2)} + v^{(3)}) + \frac{1}{6}\Delta t L(v^{(3)}). \end{cases} \quad (32)$$

This concludes the description of our MM-WENO schemes, up to discussing the specifics of the WENO reconstructions.

4 Specific WENO5 reconstructions needed by our MM-WENO schemes

In this section, we work out in detail the formally fifth order reconstructions needed for our MM-WENO schemes that use a full set of AV moments \bar{u}_i defined in (2) over each grid element and PV moments $u_{i+1/2}$ defined in (3) at each grid point. We identify the moments used in the various reconstructions by using ‘‘p’’ to denote a PV moment and ‘‘A’’ for an AV moment. We follow the general procedure described in Section 2. Our goal is to define reconstructions approximating to $\mathcal{O}(\Delta x^5)$ using a compact stencil (to reduce numerical diffusion).

4.1 Reconstruction of a point value at $x_{i+1/2}$ from pAAAp

In this subsection we reconstruct approximations to $u(x_{i+1/2})$ needed in (20) for solving the AV evolution equation (18). For $u_{i+1/2}^-$, it seems natural to use the multi-moments $\{u_{i-3/2}, \bar{u}_{i-1}, \bar{u}_i, \bar{u}_{i+1}, u_{i+3/2}\}$ defined over the spatial domain $[x_{i-3/2}, x_{i+3/2}]$, which are divided into the three stencils

$$S_1 = \{u_{i-3/2}, \bar{u}_{i-1}, \bar{u}_i\}, \quad S_2 = \{\bar{u}_{i-1}, \bar{u}_i, \bar{u}_{i+1}\}, \quad S_3 = \{\bar{u}_i, \bar{u}_{i+1}, u_{i+3/2}\}.$$

We first define over each stencil S_j its quadratic polynomial q_j matching the multi-moments, and we compute the smoothness indicators. We use the re-mapping idea of Subsection 2.2 for each stencil. In this case, it seems natural to us to re-map onto single moment AVs defined on an extended grid over $[x_{i-2}, x_{i+2}]$. The re-mapping is illustrated in Fig. 1. We remark that some people may prefer to re-map to PV moments, which is fine, since there is no difference in the final results. The same polynomials q_j are generated, just represented in a different basis.

Stencil S_1 , pAA. For the left stencil S_1 , the quadratic polynomial $q_1(x)$ is defined by matching the multi-moments $\{u_{i-2}, \bar{u}_{i-1}, \bar{u}_i\}$. In this case, the natural basis for the vector space of quadratic polynomials is given by $\{\phi_1^1, \phi_2^1, \phi_3^1\}$, where

$$\phi_j^1(x_{i-3/2}) = \delta_{1,j} \quad \text{and} \quad \frac{1}{\Delta x} \int_{E_{i+k-3}} \phi_j^1(x) dx = \delta_{jk}, \quad k = 2, 3, \quad j = 1, 2, 3,$$

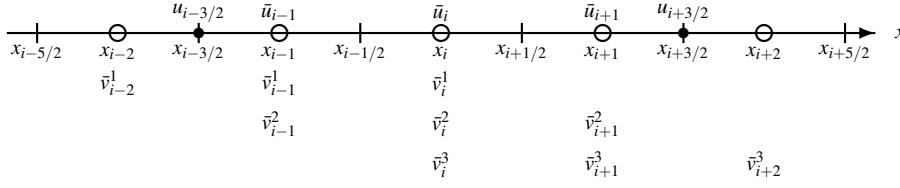


Fig. 1 The re-mapping process for pAAAp. Three AVs (circles) \bar{u}_{i-1} , \bar{u}_i , and \bar{u}_{i+1} and two PVs (dots) $u_{i-3/2}$ and $u_{i+3/2}$ are re-mapped to three stencil sets of AVs $\{\bar{v}_{i-2}^1, \bar{v}_{i-1}^1 = \bar{u}_{i-1}, \bar{v}_i^1 = \bar{u}_i\}$, $\{\bar{v}_{i-1}^2 = \bar{u}_{i-1}, \bar{v}_i^2 = \bar{u}_i, \bar{v}_{i+1}^2 = \bar{u}_{i+1}\}$, and $\{\bar{v}_i^3 = \bar{u}_i, \bar{v}_{i+1}^3 = \bar{u}_{i+1}, \bar{v}_{i+2}^3\}$.

so that $q_1(x) = u_{i-3/2}\phi_1^1(x) + \bar{u}_{i-1}\phi_2^1(x) + \bar{u}_i\phi_3^1(x)$. We want to map the multi-moments $\{u_{i-3/2}, \bar{u}_{i-1}, \bar{u}_i\}$ to the single AV moments $\{\bar{v}_{i-2}^1, \bar{v}_{i-1}^1, \bar{v}_i^1\}$, so we define the standard single moment basis $\{\Phi_1^1, \Phi_2^1, \Phi_3^1\}$ by the conditions

$$\frac{1}{\Delta x} \int_{E_{i+k-3}} \Phi_j^1(x) dx = \delta_{jk}, \quad j, k = 1, 2, 3.$$

Then we can write $q_1(x) = \bar{v}_{i-2}^1\Phi_1^1(x) + \bar{v}_{i-1}^1\Phi_2^1(x) + \bar{v}_i^1\Phi_3^1(x)$ as in the classic, single moment WENO framework. We can easily compute the change of basis matrix B as

$$\begin{bmatrix} \phi_1^1(x) \\ \phi_2^1(x) \\ \phi_3^1(x) \end{bmatrix} = B_{\text{pAA}}^A \begin{bmatrix} \Phi_1^1(x) \\ \Phi_2^1(x) \\ \Phi_3^1(x) \end{bmatrix}, \quad B_{\text{pAA}}^A = \frac{1}{2} \begin{bmatrix} 6 & 0 & 0 \\ -5 & 2 & 0 \\ 1 & 0 & 2 \end{bmatrix}, \quad (33)$$

and so the re-mapped moments are given by $\mathbf{v} = B_{\text{pAA}}^{A,T} \mathbf{u}$, i.e.,

$$\bar{v}_{i-2}^1 = 3u_{i-3/2} + \frac{1}{2}(\bar{u}_i - 5\bar{u}_{i-1}), \quad \bar{v}_{i-1}^1 = \bar{u}_{i-1}, \quad \bar{v}_i^1 = \bar{u}_i. \quad (34)$$

The classic WENO case now gives us the coefficients in the stencil polynomial as $\{\frac{1}{3}, -\frac{7}{6}, \frac{11}{6}\}$, and the result is that

$$q_1(x_{i+1/2}) = \frac{1}{3}\bar{v}_{i-2}^1 - \frac{7}{6}\bar{v}_{i-1}^1 + \frac{11}{6}\bar{v}_i^1 = u_{i-3/2} - 2\bar{u}_{i-1} + 2\bar{u}_i. \quad (35)$$

Moreover, we have that in terms of the re-mapped AVs, the smoothness indicator (10), which here is $IS_1^i(\Delta x)$, is known to be

$$IS_1^i = \frac{13}{12}(\bar{v}_{i-2}^1 - 2\bar{v}_{i-1}^1 + \bar{v}_i^1)^2 + \frac{1}{4}(\bar{v}_{i-2}^1 - 4\bar{v}_{i-1}^1 + 3\bar{v}_i^1)^2. \quad (36)$$

Stencil S_2 , AAA. The middle stencil S_2 requires no mapping to relate it to the classic WENO case, which gives us that

$$q_2(x_{i+1/2}) = -\frac{1}{6}\bar{u}_{i-1} + \frac{5}{6}\bar{u}_i + \frac{1}{3}\bar{u}_{i+1} \quad (37)$$

and that

$$IS_2^i = \frac{13}{12}(\bar{u}_{i-1} - 2\bar{u}_i + \bar{u}_{i+1})^2 + \frac{1}{4}(\bar{u}_{i-1} - \bar{u}_{i+1})^2. \quad (38)$$

Stencil S_3 , AAP. For the right stencil S_3 , the quadratic polynomial $q_3(x)$ is defined by matching the multi-moments $\{\bar{u}_i, \bar{u}_{i+1}, u_{i+3/2}\}$. We map these to the single AV moments $\{\bar{v}_i^3, \bar{v}_{i+1}^3, \bar{v}_{i+2}^3\}$ entirely analogous to the case for pAA. The result is that

$$B_{\text{AAP}}^A = \frac{1}{2} \begin{bmatrix} 2 & 0 & 1 \\ 0 & 2 & -5 \\ 0 & 0 & 6 \end{bmatrix}, \quad (39)$$

so the re-mapped moments are

$$\bar{v}_i^3 = \bar{u}_i, \quad \bar{v}_{i+1}^3 = \bar{u}_{i+1}, \quad \bar{v}_{i+2}^3 = 3u_{i+3/2} + \frac{1}{2}(\bar{u}_i - 5\bar{u}_{i+1}). \quad (40)$$

The coefficients $\{\frac{1}{3}, \frac{5}{6}, -\frac{1}{6}\}$ are used in the classic linear reconstruction, so

$$q_3(x_{i+1/2}) = \frac{1}{3}\bar{v}_i^3 + \frac{5}{6}\bar{v}_{i+1}^3 - \frac{1}{6}\bar{v}_{i+2}^3 = \frac{1}{4}\bar{u}_i + \frac{5}{4}\bar{u}_{i+1} - \frac{1}{2}u_{i+3/2}. \quad (41)$$

Moreover, in terms of the re-mapped moments,

$$IS_3^i = \frac{13}{12}(\bar{v}_i^3 - 2\bar{v}_{i+1}^3 + \bar{v}_{i+2}^3)^2 + \frac{1}{4}(3\bar{v}_i^3 - 4\bar{v}_{i+1}^3 + \bar{v}_{i+2}^3)^2. \quad (42)$$

Now that we have determined $q_j(x_{i+1/2})$ and computed the smoothness indicators, we turn to a determination of the linear weights. The fifth order accurate quartic polynomial that matches all five multi-moments, evaluated at the target point, is given by

$$q(x_{i+1/2}) = \frac{1}{9}u_{i-3/2} - \frac{8}{27}\bar{u}_{i-1} + \frac{19}{27}\bar{u}_i + \frac{19}{27}\bar{u}_{i+1} - \frac{2}{9}u_{i+3/2}.$$

It is easy to see that the linear weights $\{\gamma_1 = 1/9, \gamma_2 = 4/9, \gamma_3 = 4/9\}$ give

$$q(x_{i+1/2}) = \gamma_1 q_1(x_{i+1/2}) + \gamma_2 q_2(x_{i+1/2}) + \gamma_3 q_3(x_{i+1/2}),$$

and so the WENO reconstruction works in this case. Of course to avoid discontinuities within the WENO framework, we modify these linear weights with the smoothness indicators (10), which have been computed above for each stencil. That is, for the nonlinear weights (11),

$$u_{i+1/2}^- := \tilde{\gamma}_1 q_1(x_{i+1/2}) + \tilde{\gamma}_2 q_2(x_{i+1/2}) + \tilde{\gamma}_3 q_3(x_{i+1/2}). \quad (43)$$

In summary, the core of the re-mapping procedure was to find the transformation matrix B between multi-moment and single moment basis functions, and once this was accomplished, standard formula from the classic linear reconstruction procedures via single moments could be used for computing the stencil polynomials and smoothness indicators. Because the AV single moments are defined locally for each stencil, each stencil had to be treated individually, and the determination of the global WENO linear weights had to be done for the case at hand without reference to standard formula.

The stencil for computing $u_{i+1/2}^+$ from $\{u_{i-1/2}, \bar{u}_i, \bar{u}_{i+1}, \bar{u}_{i+2}, u_{i+5/2}\}$ is also of the type pAAAp, but with the x -axis reversed. The three stencils for WENO reconstruction are

$$S_1 = \{u_{i-1/2}, \bar{u}_i, \bar{u}_{i+1}\}, \quad S_2 = \{\bar{u}_i, \bar{u}_{i+1}, \bar{u}_{i+2}\}, \quad S_3 = \{\bar{u}_{i+1}, \bar{u}_{i+2}, u_{i+5/2}\},$$

the three stencil polynomials and smoothness indicators are defined by symmetry to the results (33)–(43) above, and the linear weights are $\{4/9, 4/9, 1/9\}$.

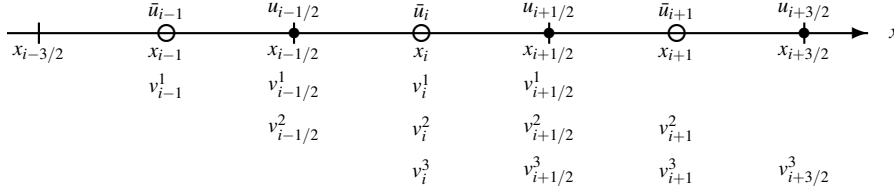


Fig. 2 The re-mapping process for ApApAp. Three AVs \bar{u}_{i-1} , \bar{u}_i , and \bar{u}_{i+1} (circles) and three PVs $u_{i-1/2}$, $u_{i+1/2}$, and $u_{i+3/2}$ (dots) are re-mapped to three stencils of four PVs v_i^j each, but on a grid refined by half.

4.2 Reconstruction of a derivative value at $x_{i+1/2}$ from ApApAp and pApApA

In this subsection we reconstruct approximations to $u_x(x_{i+1/2})$ needed for the MM-WENO-HJ scheme in (22) for solving the PV evolution equation (19). Again, our goal is to reconstruct an $\mathcal{O}(\Delta x^5)$ approximation using a compact stencil. For $u_{x_{i+1/2}}^-$, we need a large stencil of six degrees of freedom to obtain a fifth order accurate point value of the derivative u_x at $x_{i+1/2}$, so it seems natural in this case to use all the multi-moments consecutively ordered. We choose ApApAp consisting of three AVs interleaved with three PVs and divided into the three stencils

$$S_1 = \{\bar{u}_{i-1}, u_{i-1/2}, \bar{u}_i, u_{i+1/2}\}, \quad S_2 = \{u_{i-1/2}, \bar{u}_i, u_{i+1/2}, \bar{u}_{i+1}\}, \\ S_3 = \{\bar{u}_i, u_{i+1/2}, \bar{u}_{i+1}, u_{i+3/2}\}.$$

As illustrated in Fig. 2, it is convenient to map these multi-moments to three sets of four PVs,

$$\{v_{i-1}^1, v_{i-1/2}^1, v_i^1, v_{i+1/2}^1\}, \quad \{v_{i-1/2}^2, v_i^2, v_{i+1/2}^2, v_{i+1}^2\}, \quad \{v_i^3, v_{i+1/2}^3, v_{i+1}^3, v_{i+3/2}^3\},$$

respectively, defined over a refined grid on $[x_{i-1}, x_{i+3/2}]$ with half-sized elements. For WENO, we need to determine the derivative point value of three cubic polynomials defined over the three stencils, and then take a (non)linearly weighted sum that matches the corresponding value of a quintic polynomial (if this is possible independent of the multi-moments).

Stencil S_1 , ApAp. The change of basis matrix from the left stencil of multi-moments to the PVs is computed to be

$$B_{\text{ApAp}}^{\text{p}} = \frac{1}{4} \begin{bmatrix} 3 & 0 & 0 & 0 \\ 3 & 4 & -1 & 0 \\ -3 & 0 & 6 & 0 \\ 1 & 0 & -1 & 4 \end{bmatrix}, \quad (44)$$

and so

$$v_{i-1}^1 = \frac{3}{4}(\bar{u}_{i-1} - \bar{u}_i) + \frac{1}{4}(3u_{i-1/2} + u_{i+1/2}), \quad v_{i-1/2}^1 = u_{i-1/2}, \\ v_i^1 = \frac{3}{2}\bar{u}_i - \frac{1}{4}(u_{i-1/2} + u_{i+1/2}), \quad v_{i+1/2}^1 = u_{i+1/2}. \quad (45)$$

The left cubic polynomial can be determined by classical formula for the PVs (or it can be determined directly), giving

$$q_{1,x}(x_{i+1/2}) = \frac{1}{3} \frac{\Delta^+ v_{i-1}^1}{\Delta x/2} - \frac{7}{6} \frac{\Delta^+ v_{i-1/2}^1}{\Delta x/2} + \frac{11}{6} \frac{\Delta^+ v_i^1}{\Delta x/2}, \quad (46)$$

as in [12], where

$$\Delta^+ v_k = v_{k+1/2} - v_k \quad \text{and} \quad \Delta^+ v_{k-1/2} = v_k - v_{k-1/2}$$

are the forward differences on the half-sized grid. Finally, the smoothness indicator (10) is defined as $IS_j^{i+1/4}(\Delta x/2)$, and standard formula give that

$$IS_1^{i+1/4} = \frac{13}{12} \left(\frac{\Delta^+ v_{i-1}^1}{\Delta x/2} - 2 \frac{\Delta^+ v_{i-1/2}^1}{\Delta x/2} + \frac{\Delta^+ v_i^1}{\Delta x/2} \right)^2 + \frac{1}{4} \left(\frac{\Delta^+ v_{i-1}^1}{\Delta x/2} - 4 \frac{\Delta^+ v_{i-1/2}^1}{\Delta x/2} + 3 \frac{\Delta^+ v_i^1}{\Delta x/2} \right)^2. \quad (47)$$

Stencil S_2 , pApA. The change of basis matrix from the middle stencil of multi-moments to the PVs is, by symmetry to the Stencil S_1 ,

$$B_{pApA}^p = \frac{1}{4} \begin{bmatrix} 4 & -1 & 0 & 1 \\ 0 & 6 & 0 & -3 \\ 0 & -1 & 4 & 3 \\ 0 & 0 & 0 & 3 \end{bmatrix}, \quad (48)$$

and so the PV moments are

$$\begin{aligned} v_{i-1/2}^2 &= u_{i-1/2}, & v_i^2 &= \frac{3}{2} \bar{u}_i - \frac{1}{4} (u_{i-1/2} + u_{i+1/2}), \\ v_{i+1/2}^2 &= u_{i+1/2}, & v_{i+1}^2 &= -\frac{3}{4} (\bar{u}_i - \bar{u}_{i+1}) + \frac{1}{4} (u_{i-1/2} + 3u_{i+1/2}). \end{aligned} \quad (49)$$

This leads to the middle cubic value at $x_{i+1/2}$ being

$$q_{2,x}(x_{i+1/2}) = -\frac{1}{6} \frac{\Delta^+ v_{i-1/2}^2}{\Delta x/2} + \frac{5}{6} \frac{\Delta^+ v_i^2}{\Delta x/2} + \frac{1}{3} \frac{\Delta^+ v_{i+1/2}^2}{\Delta x/2}, \quad (50)$$

and the smoothness indicator evaluating to

$$IS_2^{i+1/4} = \frac{13}{12} \left(\frac{\Delta^+ v_{i-1/2}^2}{\Delta x/2} - 2 \frac{\Delta^+ v_i^2}{\Delta x/2} + \frac{\Delta^+ v_{i+1/2}^2}{\Delta x/2} \right)^2 + \frac{1}{4} \left(\frac{\Delta^+ v_{i-1/2}^2}{\Delta x/2} - \frac{\Delta^+ v_{i+1/2}^2}{\Delta x/2} \right)^2. \quad (51)$$

Stencil S_3 , ApAp. The right cubic polynomials $q_{i+1}(x)$ also belongs to the case ApAp, but the target point $x_{i-1/2}$ location within the stencil differs from that of stencil S_1 . The change of basis matrix is the same as for S_1 , giving the PV moments as

$$\begin{aligned} v_i^3 &= \frac{3}{4} (\bar{u}_i - \bar{u}_{i+1}) + \frac{1}{4} (3u_{i+1/2} + u_{i+3/2}), & v_{i+1/2}^3 &= u_{i+1/2}, \\ v_{i+1}^3 &= \frac{3}{2} \bar{u}_{i+1} - \frac{1}{4} (u_{i+1/2} + u_{i+3/2}), & v_{i+3/2}^3 &= u_{i+3/2}. \end{aligned} \quad (52)$$

But now

$$q_{3,x}(x_{i+1/2}) = \frac{1}{3} \frac{\Delta^+ v_i^3}{\Delta x/2} + \frac{5}{6} \frac{\Delta^+ v_{i+1/2}^3}{\Delta x/2} - \frac{1}{6} \frac{\Delta^+ v_{i+1}^3}{\Delta x/2} \quad (53)$$

and

$$IS_3^{i+1/4} = \frac{13}{12} \left(\frac{\Delta^+ v_i^3}{\Delta x/2} - 2 \frac{\Delta^+ v_{i+1/2}^3}{\Delta x/2} + \frac{\Delta^+ v_{i+1}^3}{\Delta x/2} \right)^2 + \frac{1}{4} \left(3 \frac{\Delta^+ v_i^3}{\Delta x/2} - 4 \frac{\Delta^+ v_{i+1/2}^3}{\Delta x/2} + \frac{\Delta^+ v_{i+1}^3}{\Delta x/2} \right)^2. \quad (54)$$

The full set of six multi-moments can be matched by a polynomial $q(x)$ of degree five, giving an $\mathcal{O}(\Delta x^5)$ approximation of the derivative $q_x(x_{i+1/2}) \approx u_x(x_{i+1/2})$. We can compute this polynomial directly, or map to six PVs and invoke the results of [12]. Trying to match $q_x(x_{i+1/2}) = \gamma_1 q_{1,x}(x_{i+1/2}) + \gamma_2 q_{2,x}(x_{i+1/2}) + \gamma_3 q_{3,x}(x_{i+1/2})$ shows that the linear weights exist, and they are $\{\gamma_1 = 1/9, \gamma_2 = 5/9, \gamma_3 = 3/9\}$. Thus, using the smoothness indicators and nonlinear weights, we have the approximation

$$u_{x,i+1/2}^- := \tilde{\gamma}_1 q_{1,x}(x_{i+1/2}) + \tilde{\gamma}_2 q_{2,x}(x_{i+1/2}) + \tilde{\gamma}_3 q_{3,x}(x_{i+1/2}). \quad (55)$$

The large stencil for computing $u_{x,i+1/2}^+$ is $\{u_{i-1/2}, \bar{u}_i, u_{i+1/2}, \bar{u}_{i+1}, u_{i+3/2}, \bar{u}_{i+2}\}$ which is a type of pApApA. The three smaller stencils for WENO reconstruction are

$$S_1 = \{u_{i-1/2}, \bar{u}_i, u_{i+1/2}, \bar{u}_{i+1}\}, \quad S_2 = \{\bar{u}_i, u_{i+1/2}, \bar{u}_{i+1}, u_{i+3/2}\}, \\ S_3 = \{u_{i+1/2}, \bar{u}_{i+1}, u_{i+3/2}, \bar{u}_{i+2}\},$$

and the results are similar to the above and given by symmetry. For example, the linear weights are simply $\{\gamma_1^+ = 3/9, \gamma_2^+ = 5/9, \gamma_3^+ = 1/9\}$. In terms of the three stencil polynomials $q_j^+(x_{i+1/2})$ and corresponding smoothness indicators,

$$u_{x,i+1/2}^+ := \tilde{\gamma}_1^+ q_{1,x}^+(x_{i+1/2}) + \tilde{\gamma}_2^+ q_{2,x}^+(x_{i+1/2}) + \tilde{\gamma}_3^+ q_{3,x}^+(x_{i+1/2}). \quad (56)$$

Remark. We could have chosen $\{\bar{u}_i, u_{i+1/2}, \bar{u}_{i+1}, u_{i+3/2}, \bar{u}_{i+2}, u_{i+5/2}\}$ as our stencil for computing $u_{x,i+1/2}^+$ since it is a type of ApApAp, the same as the stencil for computing $u_{x,i+1/2}^-$. But this choice results in linear weights $\{20/45, 28/45, -3/45\}$, which contains a negative weight that we would prefer to avoid.

4.3 Reconstruction of a derivative from point values at $x_{i+1/2 \pm 1/4}$ from pApAp and ApApA

The target functional $\mathcal{L}(u)$ needed in (27)–(29) for an FD-WENO scheme [16] is difficult to describe. Given the function $f(u(x), x)$, the idea is to rewrite it as the sliding average of another function $h(x)$ over our half-refined grid, which is to say

$$f(u(x), x) = \frac{2}{\Delta x} \int_{x-\Delta x/4}^{x+\Delta x/4} h(\xi) d\xi,$$

so that

$$f_x(x_{i+1/2}) = \frac{2}{\Delta x} [h(x_{i+3/4}) - h(x_{i+1/4})]. \quad (57)$$

The problem is that $h(x)$ is not uniquely defined; however, it can be uniquely defined if we ask that $h(x)$ be approximated by a polynomial.

As illustrated in Fig. 3, two AVs and three PVs on $[x_{i-1/2}, x_{i+3/2}]$ are divided into the three stencils

$$S_1 = \{u_{i-1/2}, \bar{u}_i, u_{i+1/2}\}, \quad S_2 = \{\bar{u}_i, u_{i+1/2}, \bar{u}_{i+1}\}, \quad S_3 = \{u_{i+1/2}, \bar{u}_{i+1}, u_{i+3/2}\}.$$

We re-map each stencil to PVs defined on the half-refined grid. For the reconstruction, following Shu [16], we view $h(x)$ as a polynomial whose AV moments are given by point values of $f(u)$, but only at the grid points. That is,

$$\bar{h}_k := \frac{2}{\Delta x} \int_{x_{k-1/4}}^{x_{k+1/4}} h(\xi) d\xi = f(u(x_k), x_k), \quad k = i, i+1/2.$$

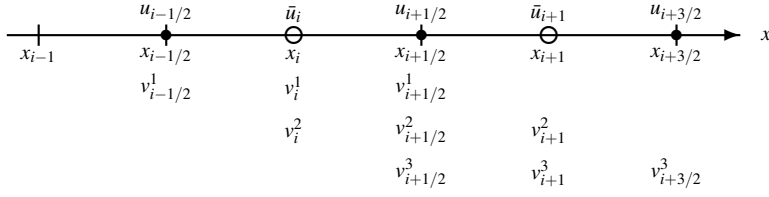


Fig. 3 The re-mapping process for pApAp. Two AVs \bar{u}_i and \bar{u}_{i+1} (circles) and three PVs $u_{i-1/2}$, $u_{i+1/2}$ and $u_{i+3/2}$ (dots) are re-mapped to three stencils of three PVs v_i^j each, but defined on a grid refined by half. We view these v_i^j as AVs of the sliding average function $h(x)$ centered at the grid points.

Then $\{\bar{h}_{i-1/2}, \bar{h}_i, \bar{h}_{i+1/2}, \bar{h}_{i+1}, \bar{h}_{i+3/2}\}$ are reconstructed in the standard way to define an $\mathcal{O}(\Delta x^5)$ approximation of $h(x_{i+3/4})$; that is, we have high order WENO reconstruction of the well-defined linear functional $\mathcal{L}(u) := h(x_{i+3/4})$. This and a reconstruction to $x_{i-1/4}$ will be used to give an accurate derivative in (57). So the strategy is to convert our multi-moments to PVs of $u(x)$, evaluate f at these PVs, and then to view these function values as AVs of $h(x)$, which we finally reconstruct to the target point.

Stencil S_1 , pAp. The change of basis matrix from the multi-moments to PVs for the left stencil can be computed as

$$B_{\text{pAp}}^{\text{p}} = \frac{1}{4} \begin{bmatrix} 4 & -1 & 0 \\ 0 & 6 & 0 \\ 0 & -1 & 4 \end{bmatrix}, \quad (58)$$

leading to the PVs of $u(x)$ denoted by v and the corresponding AVs of $h(x)$ being

$$v_{i-1/2}^1 = u_{i-1/2}, \quad v_i^1 = \frac{3}{2}\bar{u}_i - \frac{1}{4}(u_{i-1/2} + u_{i+1/2}), \quad v_{i+1/2}^1 = u_{i+1/2}, \quad (59)$$

$$\bar{h}_k^1 = f(v_k^1, x_k), \quad k = i-1/2, i, i+1/2.$$

The left cubic polynomial for $h(x)$ can be determined for the AVs by classical formula or directly, resulting in

$$h_1(x_{i+3/4}) = \frac{1}{3}\bar{h}_{i-1/2}^1 - \frac{7}{6}\bar{h}_i^1 + \frac{11}{6}\bar{h}_{i+1/2}^1. \quad (60)$$

The smoothness indicator (10) for this case is $IS_1^{i+1/2}(\Delta x/2)$, and it is known to work out to

$$IS_1^{i+1/2} = \frac{13}{12}(\bar{h}_{i-1/2}^1 - 2\bar{h}_i^1 + \bar{h}_{i+1/2}^1)^2 + \frac{1}{4}(\bar{h}_{i-1/2}^1 - 4\bar{h}_i^1 + 3\bar{h}_{i+1/2}^1)^2. \quad (61)$$

Stencil S_2 , ApA. The middle stencil has the change of basis matrix

$$B_{\text{ApA}}^{\text{p}} = \frac{1}{8} \begin{bmatrix} 7 & 0 & -1 \\ 2 & 8 & 2 \\ -1 & 0 & 7 \end{bmatrix}, \quad (62)$$

and the PVs of $u(x)$ and the AVs of $h(x)$ being

$$v_i^2 = \frac{1}{4}u_{i+1/2} + \frac{1}{8}(7\bar{u}_i - \bar{u}_{i+1}), \quad v_{i+1/2}^2 = u_{i+1/2}, \quad v_{i+1}^2 = \frac{1}{4}u_{i+1/2} + \frac{1}{8}(-\bar{u}_i + 7\bar{u}_{i+1}),$$

$$\bar{h}_k^2 = f(v_k^2, x_k), \quad k = i, i+1/2, i+1, \quad (63)$$

leading to

$$h_2(x_{i+3/4}) = -\frac{1}{6}\bar{h}_i^2 + \frac{5}{6}\bar{h}_{i+1/2}^2 + \frac{1}{3}\bar{h}_{i+1}^2, \quad (64)$$

with the smoothness indicator

$$IS_2^{i+1/2} = \frac{13}{12}(\bar{h}_i^2 - 2\bar{h}_{i+1/2}^2 + \bar{h}_{i+1}^2)^2 + \frac{1}{4}(\bar{h}_i^2 - \bar{h}_{i+1}^2)^2. \quad (65)$$

Stencil S_3 , pAp. The right quadratic polynomial $q_{i+1}(x)$ also belongs to the case pAp, so the change of basis matrix is the same as that case and

$$\begin{aligned} v_{i+1/2}^3 &= u_{i+i/2}, & v_{i+1}^3 &= \frac{3}{2}\bar{u}_{i+1} - \frac{1}{4}(u_{i+1/2} + u_{i+3/2}), & v_{i+3/2}^3 &= u_{i+3/2}, \\ \bar{h}_k^3 &= f(v_k^3, x_k), & k &= i+1/2, i+1, i+3/2. \end{aligned} \quad (66)$$

Then we have the known reconstruction

$$h_3(x_{i+3/4}) = \frac{1}{3}\bar{h}_{i+1/2}^3 + \frac{5}{6}\bar{h}_{i+1}^3 - \frac{1}{6}\bar{h}_{i+3/2}^3, \quad (67)$$

and smoothness indicator

$$IS_3^{i+1/2} = \frac{13}{12}(\bar{h}_{i+1/2}^3 - 2\bar{h}_{i+1}^3 + \bar{h}_{i+3/2}^3)^2 + \frac{1}{4}(3\bar{h}_{i+1/2}^3 - 4\bar{h}_{i+1}^3 + \bar{h}_{i+3/2}^3)^2. \quad (68)$$

Computation of the linear weights in the WENO reconstruction is a bit more involved in this case. We first need to construct the higher order polynomial representation of $h(x)$, which requires re-mapping the full set of multi-moments to the PV moments. That is, the change of basis matrix

$$B_{\text{pApAp}}^{\text{p}} = \frac{1}{64} \begin{bmatrix} 64 & -15 & 0 & 1 & 0 \\ 0 & 93 & 0 & -3 & 0 \\ 0 & -12 & 64 & -12 & 0 \\ 0 & -3 & 0 & 93 & 0 \\ 0 & 1 & 0 & -15 & 64 \end{bmatrix} \quad (69)$$

needs to be computed, and then we have that

$$\begin{aligned} v_{i+1/2+k} &= u_{i+1/2+k}, & k &= -1, 0, 1, \\ v_i &= \frac{1}{64}(-15u_{i-1/2} + 93\bar{u}_i - 12u_{i+1/2} - 3\bar{u}_{i+1} + u_{i+3/2}), \\ v_{i+1} &= \frac{1}{64}(u_{i-1/2} - 3\bar{u}_i - 12u_{i+1/2} + 93\bar{u}_{i+1} - 15u_{i+3/2}), \\ \bar{h}_k &= f(v_k, x_k), & k &= i-1/2, i, i+1/2, i+1, i+3/2. \end{aligned} \quad (70)$$

From these AVs, we can construct in the usual way

$$h(x_{i+3/4}) = \frac{1}{30}\bar{h}_{i-1/2} - \frac{13}{60}\bar{h}_i + \frac{47}{60}\bar{h}_{i+1/2} + \frac{9}{20}\bar{h}_{i+1} - \frac{1}{20}\bar{h}_{i+3/2}, \quad (71)$$

and then determine the linear weights from matching $h(x_{i+3/4}) = \gamma_1 h_1(x_{i+3/4}) + \gamma_2 h_2(x_{i+3/4}) + \gamma_3 h_3(x_{i+3/4})$ for any set of multi-moments, which gives

$$\gamma_1 = \frac{21}{144}, \quad \gamma_2 = \frac{62}{144}, \quad \gamma_3 = \frac{61}{144}. \quad (72)$$

Of course to avoid discontinuities within the WENO framework, these are modified into the nonlinear weights using the aforementioned smoothness indicators, so

$$h_{i+3/4}^- := \tilde{\gamma}_1 h_1(x_{i+3/4}) + \tilde{\gamma}_2 h_2(x_{i+3/4}) + \tilde{\gamma}_3 h_3(x_{i+3/4}). \quad (73)$$

The stencil for computing $h_{i+3/4}^+$ is $\{\bar{u}_i, u_{i+1/2}, \bar{u}_{i+1}, u_{i+3/2}, \bar{u}_{i+2}\}$, which is the type ApApA. The three stencils for WENO reconstruction are

$$S_1 = \{\bar{u}_i, u_{i+1/2}, \bar{u}_{i+1}\}, \quad S_2 = \{u_{i+1/2}, \bar{u}_{i+1}, u_{i+3/2}\}, \quad S_3 = \{\bar{u}_{i+1}, u_{i+3/2}, \bar{u}_{i+2}\}.$$

The change of basis matrices are given in (58) and (62) above, and the process can be followed in a similar way. Representing the appropriate moments in vector form, one computes

$$\mathbf{v}^1 = B_{\text{ApA}}^{\text{p},T} \mathbf{m}^1, \quad \mathbf{v}^2 = B_{\text{pAp}}^{\text{p},T} \mathbf{m}^2, \quad \mathbf{v}^3 = B_{\text{ApA}}^{\text{p},T} \mathbf{m}^3,$$

$$\bar{h}_k^j = f(v_k^j, x_k), \quad k = i + (j-1)/2, i + j/2, i + (j+1)/2, \quad j = 1, 2, 3,$$

and then defines the point values

$$h_1^+(x_{i+3/4}) = -\frac{1}{6} \bar{h}_i^1 + \frac{5}{6} \bar{h}_{i+1/2}^1 + \frac{1}{3} \bar{h}_{i+1}^1,$$

$$h_2^+(x_{i+3/4}) = \frac{1}{3} \bar{h}_{i+1/2}^2 + \frac{5}{6} \bar{h}_{i+1}^2 - \frac{1}{6} \bar{h}_{i+3/2}^2,$$

$$h_3^+(x_{i+3/4}) = \frac{11}{6} \bar{h}_{i+1}^3 - \frac{7}{6} \bar{h}_{i+3/2}^3 + \frac{1}{3} \bar{h}_{i+2}^3,$$

and the smoothness indicators IS_j^{i+1} given by

$$IS_1^{i+1,+} = \frac{13}{12} (\bar{h}_i^1 - 2\bar{h}_{i+1/2}^1 + \bar{h}_{i+1}^1)^2 + \frac{1}{4} (\bar{h}_i^1 - 4\bar{h}_{i+1/2}^1 + 3\bar{h}_{i+1}^1)^2,$$

$$IS_2^{i+1,+} = \frac{13}{12} (\bar{h}_{i+1/2}^2 - 2\bar{h}_{i+1}^2 + \bar{h}_{i+3/2}^2)^2 + \frac{1}{4} (\bar{h}_{i+1/2}^2 - \bar{h}_{i+3/2}^2)^2,$$

$$IS_3^{i+1,+} = \frac{13}{12} (\bar{h}_{i+1}^3 - 2\bar{h}_{i+3/2}^3 + \bar{h}_{i+2}^3)^2 + \frac{1}{4} (3\bar{h}_{i+1}^3 - 4\bar{h}_{i+3/2}^3 + \bar{h}_{i+2}^3)^2,$$

leading to

$$h_{i+3/4}^+ := \tilde{\gamma}_1 h_1^+(x_{i+3/4}) + \tilde{\gamma}_2 h_2^+(x_{i+3/4}) + \tilde{\gamma}_3 h_3^+(x_{i+3/4}) \quad (74)$$

with the linear weights

$$\gamma_1 = \frac{37}{216}, \quad \gamma_2 = \frac{74}{216}, \quad \gamma_3 = \frac{105}{216}. \quad (75)$$

We also need to compute $h_{i+1/4}^\pm$. These are given by symmetry to the cases for $h_{i+3/4}^\mp$ as given already. The stencil for computing $h_{i+1/4}^+$ is $\{u_{i-1/2}, \bar{u}_i, u_{i+1/2}, \bar{u}_{i+1}, u_{i+3/2}\}$, which is a type of pApAp described above, but reversed left to right to target the point $x_{i+1/4}$ instead of $x_{i+3/4}$. Thus, e.g., the linear weights are $\{61/144, 62/144, 21/144\}$ in this case. The stencil for computing $h_{i+1/4}^-$ is $\{\bar{u}_{i-1}, u_{i-1/2}, \bar{u}_i, u_{i+1/2}, \bar{u}_{i+1}\}$ which is ApApA but again reversed right to left, so, e.g., the linear weights are $\{105/216, 74/216, 37/216\}$.

5 The re-mapping procedures using AVs and ADVs for Hermite-WENO

For completeness, in this section we show that parts of the reconstructions used in the Hermite-WENO scheme of Qiu and Shu [15] can be reduced to a standard WENO reconstructions involving AVs. That is, our re-mapping procedures allow us to view the reconstructions at the cell boundary in [15] as classic linear reconstructions.

Hermite-WENO uses AV (2) and ADV (4) multi-moments. The AV moments are evolved using (18), and the ADV moments are evolved based on the space derivative of the differential equation (16). For simplicity take $f = f(u)$ only and define $g(u, u_x) = f'(u)u_x$. Then

$$\frac{\partial u_x}{\partial t} + \frac{\partial g(u, u_x)}{\partial x} = 0, \quad x \in \mathbb{R}, t > 0, \quad (76)$$

and so the average $(\bar{u}_x)_i$ is evolved similarly to \bar{u}_i according to the semidiscrete equation

$$\frac{d(\bar{u}_x)_i}{dt} = -\frac{1}{\Delta x}(\hat{g}_{i+1/2} - \hat{g}_{i-1/2}), \quad (77)$$

where $\hat{g}_{i+1/2} = \mathcal{H}_g(u_{i+1/2}^-, u_{i+1/2}^+; u_{x,i+1/2}^-, u_{x,i+1/2}^+)$ for some numerical flux such as the Lax-Friedrichs flux. We refer to [15] for further details.

Our re-mapping procedures can be used to simplify some of the WENO reconstructions of the point values $u_{i+1/2}$ and $u_{x,i+1/2}$ needed in the scheme. We identify the moments by using ‘‘A’’ to denote an AV moment and ‘‘D’’ for an ADV moment. We denote overlapping multi-moments by enclosing them in parentheses. There are two large stencil cases to consider, (AD)A(AD) for $u_{i+1/2}$ and (AD)(AD)(AD) for $u_{x,i+1/2}$.

5.1 Fifth order re-mapping for reconstruction of a point value at $x_{i+1/2}$ from (AD)A(AD)

As in [15], we take three AVs and two ADVs on $[x_{i-3/2}, x_{i+3/2}]$ divided into the three stencils

$$\{\bar{u}_{i-1}, (\bar{u}_x)_{i-1}, \bar{u}_i\}, \quad \{\bar{u}_{i-1}, \bar{u}_i, \bar{u}_{i+1}\}, \quad \{\bar{u}_i, \bar{u}_{i+1}, (\bar{u}_x)_{i+1}\},$$

which are of the types (AD)A, AAA, and A(AD), respectively. We re-map these to AVs over an extended, full-sized grid on $[x_{i-5/2}, x_{i+5/2}]$, divided into the corresponding stencils

$$\{\bar{v}_{i-2}^1, \bar{v}_{i-1}^1, \bar{v}_i^1\}, \quad \{\bar{u}_{i-1}, \bar{u}_i, \bar{u}_{i+1}\}, \quad \{\bar{v}_i^3, \bar{v}_{i+1}^3, \bar{v}_{i+2}^3\}.$$

Once we determine the re-mapping matrix, standard reconstruction and smoothness indicator function coefficients can then be invoked for WENO reconstruction of the target linear functional $u(x_{i+1/2})$.

Stencil (AD)A. The re-mapping matrix is

$$B_{(\text{AD})\text{A}}^{\text{A}} = \begin{bmatrix} 0 & 1 & 0 \\ -2\Delta x & 0 & 0 \\ 1 & 0 & 1 \end{bmatrix}, \quad (78)$$

and it results in $\bar{v}_{i-2}^1 = -2\Delta x(\bar{u}_x)_{i-1} + \bar{u}_i$, $\bar{v}_{i-1}^1 = \bar{u}_{i-1}$, $\bar{v}_i^1 = \bar{u}_i$. Therefore, e.g., we have $q_1(x_{i+1/2}) = \frac{1}{3}\bar{v}_{i-2}^1 - \frac{7}{6}\bar{v}_{i-1}^1 + \frac{11}{6}\bar{v}_i^1 = -\frac{7}{6}\bar{u}_{i-1} + \frac{13}{6}\bar{u}_i - \frac{2}{3}\Delta x(\bar{u}_x)_{i-1}$, which agrees with [15]. The smoothness indicator $IS_1^i(\Delta x)$ is standard in terms of these AVs.

Stencil AAA. No re-mapping is needed, and $q_2(x_{i+1/2}) = -\frac{1}{6}\bar{u}_{i-1} + \frac{5}{6}\bar{u}_i + \frac{1}{3}\bar{u}_{i+1}$ and a formula for $IS_2^i(\Delta x)$ is known.

Stencil A(AD). Now the re-mapping matrix is

$$B_{A(AD)}^A = \begin{bmatrix} 1 & 0 & 1 \\ 0 & 0 & -2\Delta x \\ 0 & 1 & 0 \end{bmatrix}, \quad (79)$$

giving $\bar{v}_i^3 = \bar{u}_i$, $\bar{v}_{i+1}^3 = \bar{u}_{i+1}$, $\bar{v}_{i+2}^3 = \bar{u}_i + 2\Delta x(\bar{u}_x)_{i+1}$. Therefore, standard results determine $IS_3^i(\Delta x)$ and that $q_3(x_{i+1/2}) = \frac{1}{3}\bar{v}_i^3 + \frac{5}{6}\bar{v}_{i+1}^3 - \frac{1}{6}\bar{v}_{i+2}^3 = \frac{1}{6}\bar{u}_i + \frac{5}{6}\bar{u}_{i+1} - \frac{1}{3}\Delta x(\bar{u}_x)_{i+1}$.

Finally, Qiu and Shu [15] determined that $u(x_{i+1/2}^-) \approx u_{i+1/2}^- = \sum_{\ell=1}^3 \gamma_\ell q_\ell(x_{i+1/2})$ with the linear weights

$$\gamma_1 = \frac{9}{80}, \quad \gamma_2 = \frac{29}{80}, \quad \gamma_3 = \frac{21}{40}.$$

5.2 Sixth order re-mapping for reconstruction of a derivative at $x_{i+1/2}$ from (AD)(AD)(AD)

Now we aim to approximate a derivative value, so we need one higher order of accuracy than in the previous case. We again consider AVs and ADVs on $[x_{i-3/2}, x_{i+3/2}]$, but now we use all six, as divided into three stencils of four values each, which are

$$\{\bar{u}_{i-1}, (\bar{u}_x)_{i-1}, \bar{u}_i, (\bar{u}_x)_i\}, \quad \{\bar{u}_{i-1}, \bar{u}_i, (\bar{u}_x)_i, \bar{u}_{i+1}\}, \quad \{\bar{u}_i, (\bar{u}_x)_i, \bar{u}_{i+1}, (\bar{u}_x)_{i+1}\},$$

which are of the types (AD)(AD), A(AD)A, and (AD)(AD), respectively. We find it convenient to re-map these to PVs defined at the grid points of the full-sized grid over $[x_{i-5/2}, x_{i+5/2}]$, divided into the corresponding stencils

$$\{v_{i-5/2}^1, v_{i-3/2}^1, v_{i-1/2}^1, v_{i+1/2}^1\}, \quad \{v_{i-3/2}^2, v_{i-1/2}^2, v_{i+1/2}^2, v_{i+3/2}^2\}, \\ \{v_{i-1/2}^3, v_{i+1/2}^3, v_{i+3/2}^3, v_{i+5/2}^3\}.$$

Again, we only need to determine the re-mapping matrix, and then standard reconstruction and smoothness indicator function coefficients can then be invoked for WENO reconstruction of the target linear functional $u_x(x_{i+1/2}) = u'(x_{i+1/2})$.

Stencil (AD)(AD) extended to the left. The re-mapping matrix for (AD)(AD) when mapped to PVs extending to the left is

$$B_{(AD)(AD)}^{p,-} = \frac{1}{6} \begin{bmatrix} -69 & 3 & 3 & 3 \\ -52\Delta x & -4\Delta x & 2\Delta x & 2\Delta x \\ 75 & 3 & 3 & 3 \\ -32\Delta x & -2\Delta x & -2\Delta x & 4\Delta x \end{bmatrix}. \quad (80)$$

Standard results give $IS_1^i(\Delta x)$ and

$$q_1'(x_{i+1/2}) = \frac{1}{6\Delta x} (-2v_{i-5/2}^1 + 9v_{i-3/2}^1 - 18v_{i-1/2}^1 + 11v_{i+1/2}^1) \\ = \frac{4}{\Delta x} (\bar{u}_{i-1} - \bar{u}_i) + \frac{3}{2} (\bar{u}_x)_{i-1} + \frac{7}{2} (\bar{u}_x)_i.$$

Stencil A(AD)A. The re-mapping matrix for A(AD)A is

$$B_{A(AD)A}^p = \frac{1}{12} \begin{bmatrix} 31 & 1 & 1 & -5 \\ -14 & 10 & 10 & -14 \\ 18\Delta x & -6\Delta x & 6\Delta x & -18\Delta x \\ -5 & 1 & 1 & 31 \end{bmatrix}. \quad (81)$$

Standard results give $IS_2^i(\Delta x)$ and

$$\begin{aligned} q_2'(x_{i+1/2}) &= \frac{1}{6\Delta x} (v_{i-3/2}^2 - 6v_{i-1/2}^2 + 3v_{i+1/2}^2 + 2v_{i+3/2}^2) \\ &= \frac{1}{4\Delta x} (\bar{u}_{i-1} - 4\bar{u}_i + 3\bar{u}_{i+1}) + \frac{1}{2} (\bar{u}_x)_i. \end{aligned}$$

Stencil (AD)(AD) extended to the right. The re-mapping matrix for (AD)(AD) when mapped to PVs extending to the right is

$$B_{(AD)(AD)}^{p,+} = \frac{1}{6} \begin{bmatrix} 3 & 3 & 3 & 75 \\ -4\Delta x & 2\Delta x & 2\Delta x & 32\Delta x \\ 3 & 3 & 3 & -69 \\ -2\Delta x & -2\Delta x & 4\Delta x & 52\Delta x \end{bmatrix}. \quad (82)$$

Standard results give $IS_3^i(\Delta x)$ and

$$\begin{aligned} q_3'(x_{i+1/2}) &= \frac{1}{6\Delta x} (-2v_{i-1/2}^3 - 3v_{i+1/2}^3 + 6v_{i+3/2}^3 - v_{i+5/2}^3) \\ &= \frac{2}{\Delta x} (-\bar{u}_i + \bar{u}_{i+1}) - \frac{1}{2} (\bar{u}_x)_i - \frac{1}{2} (\bar{u}_x)_{i+1}. \end{aligned}$$

Qiu and Shu [15] determined that $u'(x_{i+1/2}^-) \approx u_{x,i+1/2}^- = \sum_{\ell=1}^3 \gamma_\ell q_\ell'(x_{i+1/2})$ with the linear weights

$$\gamma_1 = \frac{1}{18}, \quad \gamma_2 = \frac{1}{9}, \quad \gamma_3 = \frac{5}{6}.$$

6 Numerical results

In this section we present several numerical experiments to test the performance of our MM-WENO schemes. We compute discrete L^1 - and L^∞ -norm errors with respect to the center value of each grid element, i.e., by $\sum_i |u(x_i) - u_i| \Delta x$ and $\max_i |u(x_i) - u_i|$, respectively, wherein u_i is reconstructed from the discrete solution. We found it convenient to use a standard fifth order reconstruction of the AVs.

6.1 Example 1, constant linear transport

We first test our schemes in the simple case of constant linear transport as applied to

$$u_t + u_x = 0, \quad x \in [0, 2], \quad u_0(x) = 0.75 + 0.25 \sin(\pi x).$$

We denote by m the number of grid points, and so here $\Delta x = 2/m$. For this smooth problem, we observe from Table 1 a clean fifth order rate of convergence for both the MM-WENO-HJ

Table 1 Ex. 1, linear transport. Error, convergence order, and CPU time at $T = 2$ for MM-WENO schemes.

m	L_h^1 error	order	L_h^∞ error	order	CPU time (s)
MM-WENO-FV					
160	1.14295E-08	—	1.18256E-08	—	17.97
320	3.56903E-10	5.00109	3.59581E-10	5.03945	71.01
640	1.11409E-11	5.00160	1.02299E-11	5.13546	280.85
1280	3.46599E-13	5.00645	3.03977E-13	5.07268	1114.66
MM-WENO-FD					
160	1.15321E-08	—	1.18561E-08	—	20.80
320	3.60173E-10	5.00082	3.59386E-10	5.04395	82.33
640	1.12432E-11	5.00156	1.02221E-11	5.13577	326.81
1280	3.49741E-13	5.00662	3.06561E-13	5.05937	1302.63

Table 2 Ex. 1, linear transport. Error, convergence order, and CPU time at $T = 2$ for WENO schemes.

m	L_h^1 error	order	L_h^∞ error	order	CPU time (s)
WENO-FV					
160	2.15825E-08	—	2.02248E-08	—	6.33
320	6.57445E-10	5.03685	5.63459E-10	5.16567	24.23
640	1.86803E-11	5.13728	1.55357E-11	5.18065	102.87
1280	4.37526E-13	5.41600	3.51409E-13	5.46629	378.85
WENO-FD					
160	3.18758E-08	—	2.79951E-08	—	8.76
320	9.44409E-10	5.07691	7.68475E-10	5.18703	34.46
640	2.64184E-11	5.15980	2.16404E-11	5.15020	136.55
1280	6.54783E-13	5.33438	5.26463E-13	5.36125	541.98

and MM-WENO-FD schemes, as expected, using quadruple precision arithmetic. The MM-WENO-HJ scheme is more efficient in CPU time than the MM-WENO-FD scheme because the latter requires a flux splitting and, more importantly, reconstruction of two points rather than one for derivative information.

We compare our results to standard WENO schemes. In Table 2 we show results for the standard WENO finite volume (WENO-FV) which uses AV moments, and for the WENO finite difference (WENO-FD) scheme which uses PV moments. We also observe a clean fifth order rate of convergence for these two schemes. Due to the need for flux splitting, WENO-FD requires a bit more CPU time than WENO-FV.

The MM-WENO schemes in general have smaller errors for the same number of grid points for this linear test problem. However, MM-WENO uses twice as much information, since we have both AV and PV moments. The MM-WENO results are not as good as the doubled mesh WENO results. Even though this is a linear test problem, the CPU comparisons should be typical of general nonlinear problems for the given mesh size, and so we omit this information from further tests.

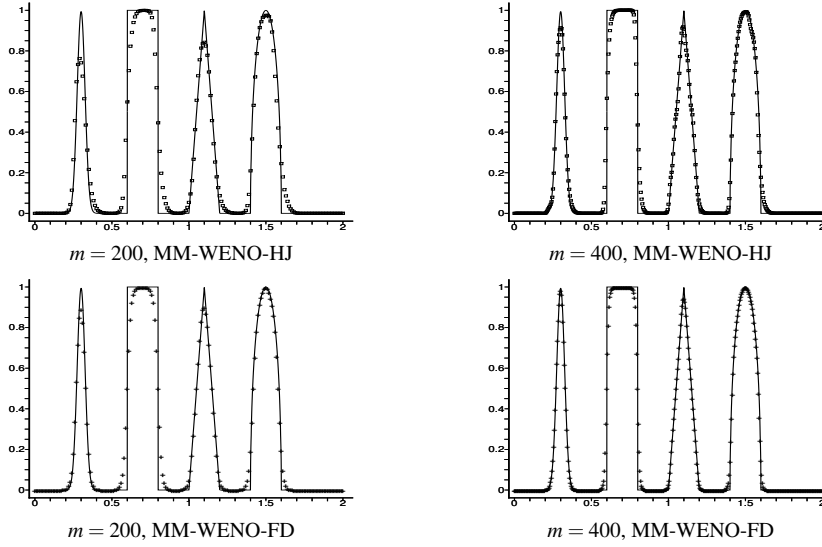
We also test our schemes with the initial condition $u_0(x) = \sin^4(\pi x)$ which generates a profile with reduced smoothness. As seen in Table 3, the convergence rates are apparently higher than fifth-order and approach sixth-order when a finer grid is used.

6.2 Example 2, Shu's linear test

We next take a standard test problem, called *Shu's linear test*, for which the initial profile is defined over $x \in [0, 2]$ and contains discontinuous jumps and smooth regions. Two sets of meshes with different resolutions, $m = 200$ and $m = 400$ grid elements, are used. Results

Table 3 Ex. 1, linear transport with $u_0 = \sin^4(\pi x)$. Error and convergence order at $T = 2$ for MM-WENO.

m	L_h^1 error	order	L_h^∞ error	order
MM-WENO-FV				
160	1.31883E-05	—	1.64663E-05	—
320	3.02135E-07	5.44791	4.17523E-07	5.30151
640	6.55731E-09	5.52594	8.73954E-09	5.57815
1280	1.28379E-10	5.67461	1.37243E-10	5.99274
MM-WENO-FD				
160	1.32020E-05	—	1.63123E-05	—
320	3.03477E-07	5.44302	4.23494E-07	5.26747
640	6.58711E-09	5.52580	8.92323E-09	5.56863
1280	1.28761E-10	5.67688	1.42574E-10	5.96779

**Fig. 4** Ex. 2, Shu's linear test. The solution using $m = 200$ and $m = 400$ grid elements and $\Delta t = 0.4\Delta x$ at time $T = 2.0$ for both schemes. The top row of graphs show results using MM-WENO-HJ (squares) and the bottom row uses MM-WENO-FD (crosses). The left column uses $m = 200$ and the right column uses $m = 400$.

at time $T = 2.0$ using $\Delta t = 0.4\Delta x = 0.8/m$ are shown in Fig. 4. It is observed that the two schemes effectively remove the spurious oscillations around the discontinuities, and are accurate for the smooth part of the solutions. The results also suggest that the MM-WENO-FD scheme is better, because it gives more symmetrical solutions to Shu's linear test.

6.3 Example 3, Burgers' equation

In the third example we test Burgers' equation with a simple initial condition to evaluate the convergence rates of the schemes for a nonlinear problem; that is, for

$$u_t + (u^2/2)_x = 0, \quad x \in (0, 2), \quad u_0(x) = 0.5 + \sin(\pi x).$$

Shocks will form at time $t = 1/\pi \approx 0.32$, so we ran the computation over gradually refined meshes up to $T = 0.25$, before the shocks are fully developed. The numerical errors and

convergence orders for the two schemes are given in Table 4. We see fifth order convergence again for this nonlinear problem. The numerical errors and convergence orders for the standard finite volume WENO5 schemes are given in Table 5. The two types of MM-WENO schemes produce smaller errors than WENO5 for the same mesh. However, as we saw previously, the MM-WENO schemes are more costly for the same mesh.

Fig. 5 shows the solutions at $T = 3/(2\pi) \approx 0.48$ after the shocks have formed. There is no numerical oscillation and both schemes perform satisfactorily.

Table 4 Ex. 3, Burgers' equation. Error and convergence order at $T = 0.25$ for the MM-WENO schemes.

m	L_h^1 error	order	L_h^∞ error	order
MM-WENO-FV				
160	6.25998E-06	—	1.74046E-04	—
320	2.31154E-07	4.75923	6.67196E-06	4.70521
640	7.93618E-09	4.86427	2.29620E-07	4.86079
1280	2.40703E-10	5.04312	7.11894E-09	5.01144
MM-WENO-FD				
160	1.65052E-05	—	4.03843E-04	—
320	6.36019E-07	4.69770	1.56218E-05	4.69216
640	2.04664E-08	4.95774	4.42326E-07	5.14231
1280	1.10577E-09	4.21013	2.00487E-08	4.46353

Table 5 Ex. 3, Burgers' equation. Error and convergence order at $T = 0.25$ for the WENO5 schemes.

m	L_h^1 error	order	L_h^∞ error	order
WENO-FV				
160	3.10975E-05	—	7.26013E-04	—
320	1.38011E-06	4.49395	3.74803E-05	4.27579
640	4.75861E-08	4.85810	1.41658E-06	4.72565
1280	1.51943E-09	4.96894	4.54978E-08	4.96047
WENO-FD				
160	3.63713E-05	—	8.56831E-04	—
320	1.51353E-06	4.58682	4.14298E-05	4.37027
640	4.84742E-08	4.96455	1.47468E-06	4.81219
1280	1.46748E-09	5.04581	4.52909E-08	5.02504

We also study Burgers' equation with a combination of a shock and a rarefaction. The initial condition is changed to

$$u_0(x) = \begin{cases} 0.5, & \text{if } x \leq 0.3 \text{ and } x > 0.75, \\ 1.0, & \text{if } 0.3 < x \leq 0.75. \end{cases}$$

With only $m = 40$ and 80 grid elements, we see good accuracy in Fig. 6. The results suggest that both schemes perform well. There is no significant difference in the numerical results of MM-WENO-HJ and MM-WENO-FD.

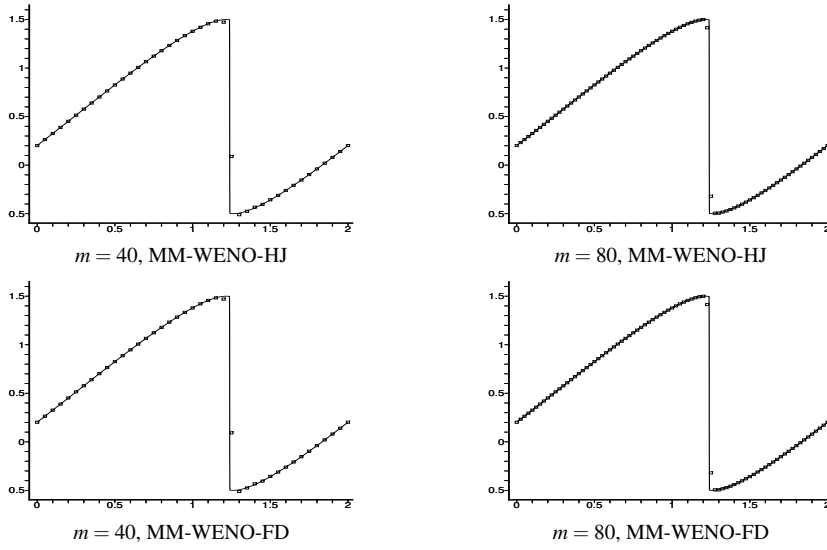


Fig. 5 Ex. 3, Burgers' equation with a shock. The solution using $m = 40$ and $m = 80$ grid elements and $\Delta t = 0.1\Delta x$ at time $T = 3/(2\pi)$. The top row of graphs show results using the MM-WENO-HJ scheme, and the bottom row uses the MM-WENO-FD scheme. The left column uses $m = 40$ and the right column uses $m = 80$.

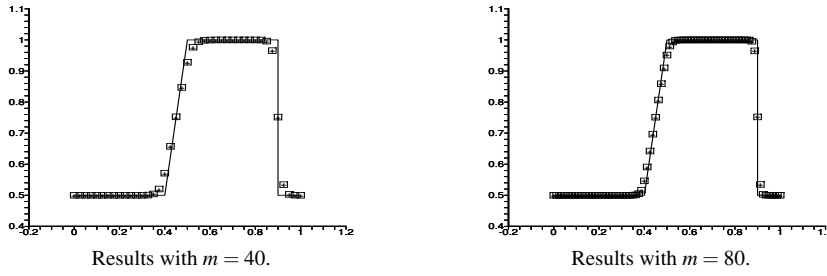


Fig. 6 Ex. 3, Burgers' equation with a shock and rarefaction. The solution using $m = 40$ (left) and $m = 80$ (right) grid elements and $\Delta t = 0.3\Delta x$ at time $T = 0.2$. The squares are results using MM-WENO-HJ, and the crosses are results using MM-WENO-FD.

6.4 Example 4, Buckley-Leverett equation

This last example for scalar conservation law (16) uses the Buckley-Leverett flux function

$$f(u) = \frac{u^2}{u^2 + (1-u)^2}$$

and involves the interaction of shocks and rarefactions. The initial condition is

$$u_0(x) = \begin{cases} 1 - 20x & \text{for } 0 \leq x \leq 0.05, \\ 0.5 & \text{for } 0.25 \leq x \leq 0.4, \\ 0 & \text{otherwise,} \end{cases} \quad (83)$$

and has two pulses that merge in time. We use $m = 40$ grid elements. The results for the two schemes and WENO5-FV are shown in Fig. 7, and the schemes handles the merging

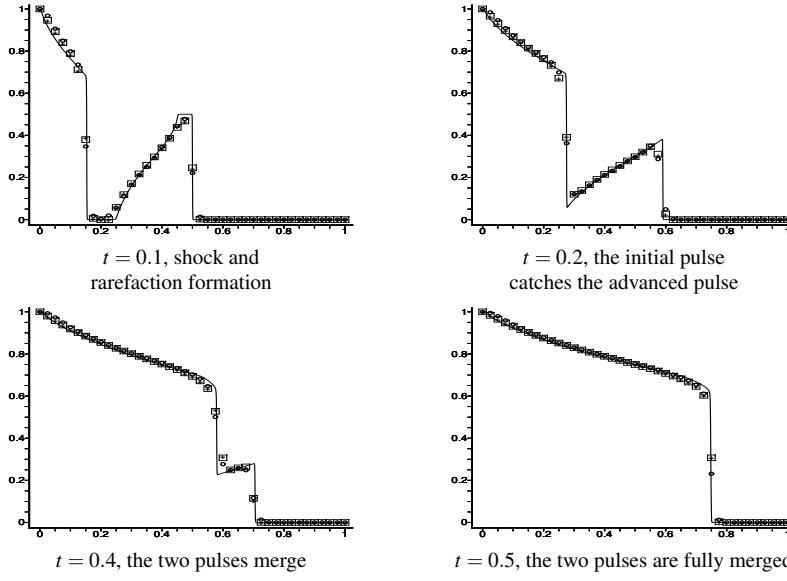


Fig. 7 Ex. 4, Buckley-Leverett equation. An interaction of shocks and rarefactions, resulting from the evolution of the initial condition of two pulses given in (83). The solid line is the reference solution, given by CWENO5 with a very small $\Delta x = 1/1280$ and $\Delta t = 1/15360$. The squares are our MM-WENO-HJ results, crosses are our MM-WENO-FD results, circles are WENO5-FV results, all using $m = 40$ and $\Delta t = 0.2\Delta x$.

of the two pulses quite well and reproduce the solution of adequate accuracy even with such a low resolution grid. As in the previous test, we see no significant difference between the MM-WENO-HJ and MM-WENO-FD schemes. The MM-WENO results are slightly better than that of WENO5-FV, but, again, the computational costs of MM-WENO are more than WENO5 for the same mesh. WENO5-FD shows a bit more numerical diffusion than WENO5-FV in this test.

7 Application to the Euler system

For a polytropic gas, the energy is $E = p/(\gamma - 1) + \rho u^2/2$, where p , ρ , and u are the pressure, density, and velocity, respectively, and γ is the adiabatic index ($\gamma = 1 + 2/f = 1.4$, where $f = 5$ is the number of degrees of freedom of each gas particle). The one-dimensional dynamics is described by the Euler equations

$$\begin{pmatrix} \rho \\ \rho u \\ E \end{pmatrix}_t + \begin{pmatrix} \rho u \\ \rho u^2 + p \\ u(E + p) \end{pmatrix}_x = 0. \quad (84)$$

To respect the characteristic structure of the system, it is usual to reconstruct the needed information from the linearized system. We expand (84) into a system of the form $U_t + A(U)U_x = 0$, that is, into

$$\begin{pmatrix} \rho \\ \rho u \\ E \end{pmatrix}_t + \begin{pmatrix} 0 & 1 & 0 \\ \frac{1}{2}(\gamma - 3)u^2 & (3 - \gamma)u & \gamma - 1 \\ \frac{1}{2}(\gamma - 1)u^3 - \frac{u(E + p)}{\rho} & \frac{(E + p)}{\rho} - (\gamma - 1)u^2 & \gamma u \end{pmatrix} \begin{pmatrix} \rho \\ \rho u \\ E \end{pmatrix}_x = 0.$$

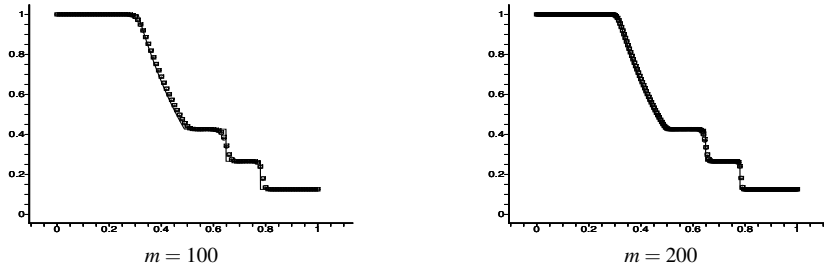


Fig. 8 Ex. 5, Sod's 1-D shock tube test. The density profile at time $T = 0.16$ using $\Delta t = 0.1\Delta x$ and $m = 100$ (left) and 200 (right) grid elements. Shown are results using MM-WENO-HJ (squares), MM-WENO-FD (crosses), and WENO5 (circles).

Being of hyperbolic type, the linearized equation can be diagonalized as $\Lambda = LA(U)(L)^{-1}$, giving

$$L \begin{pmatrix} \rho \\ \rho u \\ E \end{pmatrix}_t + \begin{pmatrix} u-c & 0 & 0 \\ 0 & u & 0 \\ 0 & 0 & u+c \end{pmatrix} L \begin{pmatrix} \rho \\ \rho u \\ E \end{pmatrix}_x = 0,$$

where $c = \sqrt{(\gamma p)/\rho}$ is the sound speed and L is the matrix formed from the eigenvectors corresponding to the three eigenvalues, $u - c$, u , and $u + c$.

For the Euler equations, all re-mapping procedures and WENO reconstructions are performed in local characteristic directions; that is, we perform the local characteristic decomposition [4] over the conserved variables for all multi-moment information first, and then we apply the re-mapping procedures and WENO reconstructions on the characteristic variables. For updating the AV and PV flux values, Roe's flux is used for approximate Riemann solvers (for details, see [11]).

7.1 Example 5, Riemann problems for the Euler equations

For this series of tests, we specify discontinuous initial conditions in terms of the primitive variables ρ , u , and p . As is typical, we only plot the numerical results for the density ρ . The other variables show comparable accuracy.

Sod's 1-D shock tube. The one-dimensional shock tube test of Sod uses the initial condition

$$\rho, u, p = \begin{cases} \rho_l = 1, u_l = 0, p_l = 1, & \text{for } x < 1/2, \\ \rho_r = 1/8, u_r = 0, p_r = 1/10, & \text{for } x > 1/2. \end{cases}$$

The results are shown in Fig. 8. Good results are obtained using $m = 100$ and 200 grid points. The quality of the numerical solutions from the MM-WENO schemes are comparable to WENO5 results.

Lax's 1-D shock tube. The one-dimensional shock tube test of Lax uses the initial condition

$$\rho, u, p = \begin{cases} \rho_l = 0.445, u_l = 0.698, p_l = 3.528, & \text{for } x < 1/2, \\ \rho_r = 0.5, u_r = 0, p_r = 0.571, & \text{for } x > 1/2. \end{cases}$$

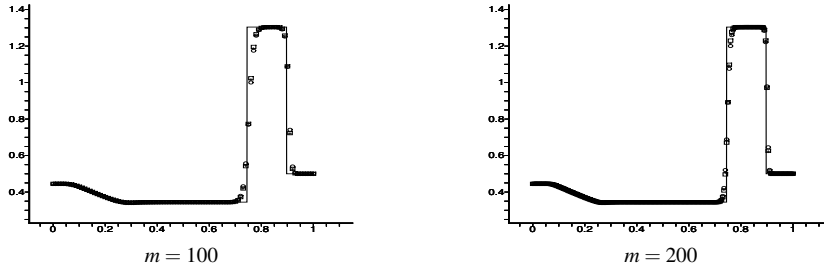


Fig. 9 Ex. 5, Lax's 1-D shock tube test. The density profile at time $T = 0.16$ using $\Delta t = 0.1\Delta x$ and $m = 100$ (left) and 200 (right) grid elements. Shown are results using MM-WENO-HJ (squares), MM-WENO-FD (crosses), and WENO5 (circles).

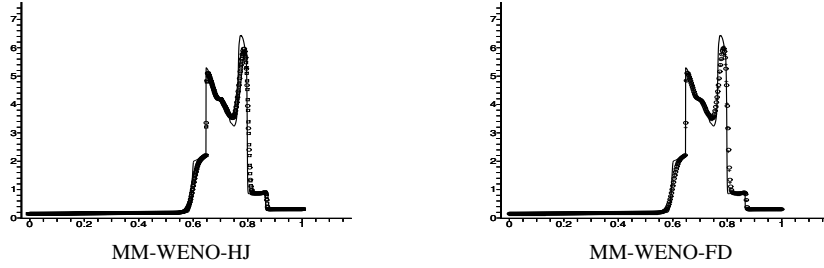


Fig. 10 Ex. 6, Woodward and Colella's double blast test. The density profile at time $T = 0.038$ using $m = 400$ grid elements. Shown are results for MM-WENO-HJ (squares, left), MM-WENO-FD (crosses, right), WENO5 (circles), and the fine resolution reference solution (solid line).

Reasonably good results are shown in Fig. 9, using $m = 100$ and 200 grid elements. There is no visible difference between the solutions of MM-WENO-HJ and MM-WENO-FD. It is also observed that both schemes get a better resolved contact discontinuity when a finer mesh is used. Similar to Sod's shock tube test, the quality of the numerical solutions from our new schemes are comparable to WENO5 results.

7.2 Example 6: Woodward and Colella's double blast test

The double blast test of Woodward and Colella uses the initial condition

$$\rho, u, p = \begin{cases} \rho_l = 1, u_l = 0, p_l = 1000, & \text{for } x < 1/10, \\ \rho_m = 1, u_m = 0, p_m = 1/100, & \text{for } 1/10 < x < 9/10, \\ \rho_r = 1, u_r = 0, p_r = 100, & \text{for } 9/10 < x. \end{cases}$$

This is a more challenging problem. Nevertheless, reasonably good results are obtained by our MM-WENO schemes using $m = 400$ grid elements, as shown in Fig. 10, which look competitive to results for the WENO5 scheme. The reference solution was computed by a MUSCL scheme with grid size $m = 4000$.

7.3 Example 7, Shu and Osher's shock interaction with entropy waves

In our final example, we consider the challenging test case of Shu and Osher [17], in which a Mach 3 shock interacts with entropy sine waves in the density. We scale the problem to

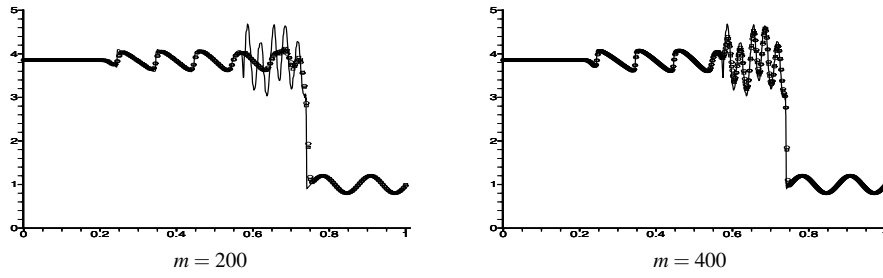


Fig. 11 Ex. 7, Shu and Osher's test with shock interacting with entropy waves. The density profile at time $T = 0.18$ using $m = 200$ and $m = 400$ grid elements. Shown are results for MM-WENO-HJ (squares), MM-WENO-FD (crosses), WENO5-FV (circles), and the fine resolution reference solution (solid line).

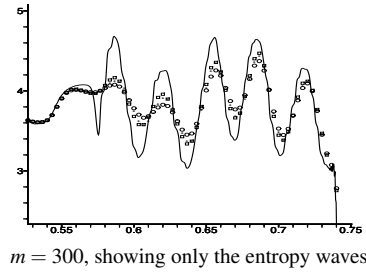


Fig. 12 Ex. 7, Shu and Osher's test with shock interacting with entropy waves. The density at $T = 0.18$ using $m = 300$ grid elements, showing only the entropy waves. Shown are results for MM-WENO-HJ (squares), MM-WENO-FD (crosses), WENO5-FV (circles), and the fine resolution reference solution (solid line).

the domain $(0, 1)$, and the initial conditions are

$$\rho, u, p = \begin{cases} \rho_l = 3.857143, u_l = 2.629369, p_l = 10.333333, & \text{for } 0 < x < 1/10, \\ \rho_r = 1 + \varepsilon \sin(5(10x - 5)), u_r = 0, p_r = 1, & \text{for } 1/10 \leq x < 1, \end{cases}$$

where $\varepsilon = 0.2$. We use $\Delta t = 0.1\Delta x$ and compute to the final time $T = 0.18$. Using the mesh sizes $m = 200$ and $m = 400$ grid elements, the results appear in Fig. 11. As is typical for this problem, $m = 200$ under resolves the entropy waves, but $m = 400$ is sufficient to capture these waves. All three methods perform similarly.

In Fig. 12 we show results for $m = 300$ grid elements. In this case, we see partial resolution of the entropy waves. The MM-WENO-HJ results are better than MM-WENO-FD, and both these are a bit better than the WENO5-FV results in this case.

8 Summary and conclusions

In Sections 2 and 3, we have presented a general approach to make WENO reconstructions applicable to the class of multi-moment numerical schemes that use different moments as the computational variables and update these simultaneously. Our approach can be viewed as a way to construct new schemes using the following steps.

1. Select the types of moments, i.e., the multi-moments, that will describe the solution.
2. Determine how each type of moment will be updated over a time step. This will determine the kinds of function values and/or derivatives that will need to be reconstructed to high order accuracy.

3. Select the large and small stencils to achieve the desired level of accuracy.
4. Determine the change of basis matrix that re-maps the discrete multi-moments on the small stencils to standard single moments, either cell average values (AVs) or point values (PVs), whichever is more convenient. Several such change of basis matrices were given above.
5. Build the stencil polynomials and the smoothness indicators from the re-mapped single moments and the coefficients used in the conventional WENO method.
6. Build the higher order polynomial over the large stencil using the full set of multi-moments and determine the linear weights needed in the reconstruction. If they do not exist, the attempt at defining a scheme fails (but see [8, 7]).
7. Using the smoothness indicators, modify the linear weights into the nonlinear weights.
8. Calculate the numerical fluxes and possibly their derivatives, as well as any other needed quantities from the WENO reconstructions.
9. Select a time-integration scheme.

Finding the change of basis matrix in Step 4 is in some sense the key, because it allows us to re-use information from conventional WENO reconstructions. We could also use information from and implement in a straightforward way other, more recent and advanced WENO schemes, like WENO-M [6] and WENO-Z [2].

In Section 3, we gave two MM-WENO schemes that follow this prescription, making the choice of using a full set of PV and AV multi-moments to achieve fifth order accuracy and increase stencil compactness. We updated the AV moments in the usual conservative way, and gave two variants for updating the PV moments. A Hamilton-Jacobi formulation of the equation [12] resulted in the MM-WENO-HJ scheme, and a more standard finite difference form [16] resulted in the MM-WENO-FD scheme. All details of the WENO reconstructions were given in Section 4.

We also pointed out that the Hermite-WENO scheme [15] can be derived using our approach. In fact, we worked out the change of basis matrix from AV and ADV moments to single moments of the type AV or PV, as convenient, in Section 5.

We can also view our approach as giving a scheme or code with the following steps.

1. Using the change of basis matrix, re-map the discrete multi-moments to the standard single moments.
 2. Build the stencil polynomials and the smoothness indicators from the re-mapped single moments and the coefficients used in the conventional WENO method.
 3. Compute the WENO reconstructions from the stencil polynomial, smoothness indicators, and the linear weights.
 4. Calculate all the numerical fluxes needed using the WENO reconstructions.
 5. Update each type of moment appropriately.
- Steps 2 and 3 are similar to what is in a standard WENO scheme. We have extended this standard procedure to a wider variety of schemes in Steps 1, 4, and 5, which provides a new path to extend the horizon of the WENO method.

The numerical tests in Sections 6 and 7 demonstrated that the two new methods have at least fifth-order accuracy as they were designed to have, and that they effectively eliminate spurious oscillations. The numerical solutions to all of the benchmark tests were of good quality and compared favorably to standard WENO5 results. The two schemes gave solutions of similar accuracy and quality in all our tests save Shu's linear test, for which the MM-WENO-FD scheme performed better. However, this is a very special linear test problem. Conversely, as noted in Subsection 3.2, the MM-WENO-FD scheme is a bit more costly than the MM-WENO-HJ scheme.

Although we limited our discussion to some representative schemes in this paper, we believe that the underlying approach given here is universally applicable. That is, we have an

easy-to-follow paradigm making WENO reconstructions easy to implement for a wide variety of numerical schemes. We note specifically that our approach can be extended straightforwardly to structured grids in two and three dimensions.

References

1. R. Akoh, S. Ii and F. Xiao, A multi-moment finite volume formulation for shallow water equations on unstructured mesh, *J. Comput. Phys.* **229** (2010) 4567–4590.
2. M. Castro, B. Costa and W.S. Don, High order weighted essentially non-oscillatory WENO-Z schemes for hyperbolic conservation laws, *J. Comput. Phys.* **230** (2011) 1766–1792.
3. C.G. Chen and F. Xiao, Shallow water model on cubed-sphere by multi-moment finite volume method, *J. Comput. Phys.* **227** (2008) 5019–5044.
4. A. Harten, B. Engquist, S. Osher and S.R. Chakravarthy, Uniformly high-order accurate essentially nonoscillatory schemes III, *J. Comput. Phys.* **71** (2) (1987) 231–303.
5. A. Harten and S. Osher, Uniformly high-order accurate nonoscillatory schemes I, *SIAM J. Numer. Anal.* **24** (2) (1987) 279–309.
6. A.K. Henrick, T.D. Aslam and J.M. Powers, Mapped weighted essentially non-oscillatory schemes: achieving optimal order near critical points, *J. Comput. Phys.*, **207** (2005) 542–567
7. C.-S. Huang and T. Arbogast, An Eulerian-Lagrangian WENO method for nonlinear conservation laws, in preparation.
8. C.-S. Huang, T. Arbogast and Ch.-H. Hung, A re-averaged WENO reconstruction and a third order CWENO scheme for hyperbolic conservation laws, *J. Comput. Phys.* **262** (2014) 291–312.
9. C.-S. Huang, T. Arbogast, J. Qiu, An Eulerian-Lagrangian WENO finite volume scheme for advection problems, *J. Comput. Phys.* **231** (11) (2012) 4028–4052, DOI 10.1016/j.jcp.2012.01.030.
10. S. Ii and F. Xiao, CIP/multi-moment finite volume method for Euler equations, a semi-Lagrangian characteristic formulation, *J. Comput. Phys.* **222** (2007) 849–871.
11. S. Ii and F. Xiao, High order multi-moment constrained finite volume method. Part I: Basic formulation, *J. Comput. Phys.* **228** (2009) 3669–3707.
12. J.-S. Jiang and D. Peng, Weighted ENO schemes for Hamilton-Jacobi equations, *SIAM J. Sci. Comput.* **21** (6) (2000) 2126–2143.
13. J.-S. Jiang and C.-W. Shu, Efficient implementation of weighted ENO schemes, *J. Comput. Phys.* **126** (1996) 202–228.
14. X. D. Liu, S. Osher and T. Chan, Weighted essentially non-oscillatory schemes, *J. Comput. Phys.* **115** (1994) 200–212.
15. J. Qiu and, C.-W. Shu, Hermite WENO schemes and their application as limiters for Runge-Kutta discontinuous Galerkin method: one-dimensional case, *J. Comput. Phys.* **193** (2003) 115–135.
16. C.-W. Shu, Essentially non-oscillatory and weighted essentially non-oscillatory schemes for hyperbolic conservation laws, ICASE–1997–65.
17. C.-W. Shu and S. Osher, Efficient implementation of essentially non-oscillatory shock capturing schemes II, *J. Comput. Phys.* **83** (1989) 32–78.
18. F. Xiao, Unified formulation for compressible and incompressible flows by using multi integrated moments I: One-dimensional inviscid compressible flow, *J. Comput. Phys.* **195** (2004) 629–654.
19. F. Xiao, R. Akoh and S. Ii, Unified formulation for compressible and incompressible flows by using multi integrated moments II: multi-dimensional version for compressible and incompressible flows, *J. Comput. Phys.* **213** (2006) 31–56.
20. F. Xiao, A. Ikebata and T. Hasegawa, Numerical simulations of free-interface fluids by a multi integrated moment method, *Computers & Structures* **83** (2005) 409–423.
21. F. Xiao, S. Ii, C.G. Chen and X.L. Li, A note on the general multi-moment constrained flux reconstruction formulation for high order schemes, *Appl. Math. Modelling* **37** (2013) 5092–5108.
22. F. Xiao and T. Yabe, Completely conservative and oscillationless semi-Lagrangian schemes for advection transportation, *J. Comput. Phys.* **170** (2001), 498–522.
23. F. Xiao, T. Yabe and T. Ito, Constructing oscillation preventing scheme for advection equation by rational function, *Comput. Phys. Commun.* **93** (1996) 1–12.
24. F. Xiao, T. Yabe, X. Peng and H. Kobayashi, Conservative and oscillation-less atmospheric transport schemes based on rational functions, *J. Geophys. Res.* **107** (D22) (2002) 4609.
25. T. Yabe and T. Aoki, A universal solver for hyperbolic equations by cubic-polynomial interpolation. 1. One-dimensional solver, *Comput. Phys. Commun.* **66** (1991) 219–232.
26. T. Yabe, F. Xiao and T. Utsumi, The constrained interpolation profile method for multiphase analysis, *J. Comput. Phys.* **169** (2001) 556–593.